ESC-TR-2010-054

Technical Report
1150

Airborne MIMO GMTI Radar

J.M. Kantor
S.K. Davis

31 March 2011

Lincoln Laboratory
MASSACHUSETTS INSTITUTE OF TECHNOLOGY
LEXINGTON, MASSACHUSETTS

Prepared for the Department of the Air Force under Contract FA8721-05-C-0002.

This report is based on studies performed at Lincoln Laboratory, a center for research operated by Massachusetts Institute of Technology. This work was sponsored by the Department of the Air Force ESC/CAA, under Contract FA8721-05-C-0002.

The 66ABW Public Affairs Office has reviewed this report, and it is releasable to the National Technical Information Service, where it will be available to the general public, including foreign nationals.

This technical report has been reviewed and is approved for publication.

FOR THE COMMANDER

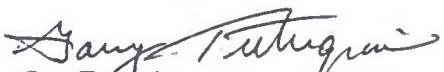

Gary Tutungian
Administrative Contracting Officer
Plans and Programs Directorate
Contracted Support Management

Massachusetts Institute of Technology
Lincoln Laboratory

Airborne MIMO GMTI Radar

J.M. Kantor
S.K. Davis
Group 105

Technical Report 1150

31 March 2011

Lexington Massachusetts

This page intentionally left blank.

EXECUTIVE SUMMARY

In recent years, multiple-input multiple-output (MIMO) techniques have been considered for their potential benefits to radar applications [1], [2], [3], [4], [5], [6], [7], [8], [9], [10], [11], [12]. Conventional phased array radars form a single coherent transmit beam and measure the backscattered response over an array of receiver phase centers. We thus call these classical systems single-input multiple-output (SIMO) systems. In a MIMO radar system, one allows for the possibility of multiple distinct waveforms being transmitted from each phase center.

In the current literature, there are two basic approaches to MIMO radar. From one perspective, the additional MIMO degrees of freedom can be used to improve scattering diversity to combat target fading. This approach relies on broadly spacing the antennas to achieve independent scattering responses across the transmit-receive pairs. The second perspective aims to enhance the angular resolution of a scatterer by coherently combining the responses across transmit-receive pairs. In order to achieve coherence in this second approach, the transmit and receive antennas must be relatively close together. It is this second perspective, the coherent MIMO radar, that we focus on in this report.

As we will see, the MIMO approach allows the use of arrays which are physically sparse, but which by separating the responses of each transmit/receive pair, extracts the same phase information that a filled array would obtain. In particular, MIMO systems can be designed with large physically sparse arrays that do not suffer from the adverse effects of grating lobes [8]. For ground moving target indicator (GMTI) radars, there are two implications of the availability of larger arrays: improved angle estimation and minimum detectable velocity (MDV). While the potential for improvement has been shown through theoretical analysis [7], [8], there is little analysis of airborne MIMO GMTI performance based on experimental data. To extend the understanding of MIMO radar beyond theoretical analysis, an airborne MIMO GMTI data collection experiment was carried out using a custom-built experimental MIMO testbed. Analysis of the experimental data is the principal focus of this report.

The report is organized as follows. In Section 1, we give an overview of the theory behind MIMO radar. In Section 2, we highlight some issues concerning the choice of waveform sets for MIMO radar. This builds heavily on the previous work in [10] and especially [13] concerning the limitations on GMTI performance of realistic MIMO waveforms. In Section 4, we describe the recent airborne experiment that was conducted aimed at demonstrating the MIMO GMTI performance improvements using a small-scale experimental testbed. In Section 5, we describe the signal processing chain developed to process our experimental MIMO radar data. Most of the focus in this section is on adaptive calibration of our system. In Section 6, we analyze the performance of the experimental MIMO GMTI system and compare it to the performance of the testbed operated in a conventional GMTI mode. In Section 7, we discuss some issues regarding how to fairly compare the performance of MIMO and SIMO GMTI systems. In Section 8, we discuss some avenues for future research. Finally, we provide a summary and conclusions in Section 9.

This page intentionally left blank.

ACKNOWLEDGMENTS

The authors thank Dan Bliss, Keith Forsythe, Jerry Benitz, Dan Rabideau, Larry Horowitz, and Paul Monticciolo for many helpful discussions on the experiment and data analysis for this report. This work is a continuation of an earlier study by the MIMO GMTI radar team which included Dan Bliss, Keith Forsythe, Dan Rabideau, Larry Horowitz, Pamela Evans, Glenn Fawcett, and Shawn Kraut. Dave Goldfein also provided many helpful suggestions for the design of a MIMO radar testbed.

The MIMO radar testbed was realized on a short time line and budget thanks to the dedicated efforts of many people. The authors thank Lee Duter and Brad Perry for designing the RF front end; Sean Tobin and Emil Eastburn for designing and testing the control logic; Peter Priestner and Larry Artz for the long hours spent building the RF front end and control logic; Jeff Novak, John Mann, and John Stueve for many consultations on the digital transmitter and receiver hardware; Alan Fenn, Peter Hurst, Ed LeFave, John Sandora, and Tom Alosso for designing, building, and characterizing the MIMO radar testbed array; Robert Murray, Kenn McKenna, Tom Matte, Rick Coveno, and Ed LeFave for installations on the aircraft; and Robert Murray, Kenn McKenna, and Andy Guertin for the aircraft support during the installation and testing.

Finally, the authors thank the MIMO radar team members and the following participants who endured two hot August days at Ft Devens to collect the experimental data for this report: Peter Priestner (ground equipment), Larry Artz (ground equipment), Sean Tobin (radar operator), Emil Eastburn (radar operator), Shourov Chatterji (ground activities), Daniel Gilbert (ground activities), David Barrett (ground activities), Rowland O'Flaherty (ground activities), Paul Monticciolo (ground activities), Daniel Bliss (ground activities), Keith Forsythe (ground activities), Trevor Chamberlain (video), Todd Lardy (pilot), and Stephen Pantano (pilot).

This page intentionally left blank.

TABLE OF CONTENTS

LIST OF ILLUSTRATIONS

LIST OF TABLES

This page intentionally left blank.

1. INTRODUCTION

Conventional phased-array radars form a single coherent transmit beam and measure the backscattered response over an array of receiver phase centers. We refer to conventional radars as single-input multiple-output (SIMO) radars. The idea behind a multiple-input multiple-output (MIMO) radar is that multiple independent waveforms are transmitted simultaneously from distinct phase centers. In this work, we focus on the case in which the transmitters and receivers are in close proximity so that coherent scattering can be observed across the transmit-receive pairs. By extracting the phase information contained in each transmit-receive path, a MIMO system can synthesize a virtual array larger than the physical array and with more degrees of freedom. In particular as we will see, it is possible to use physically sparse arrays to produce long filled virtual arrays.

Although MIMO can be considered for many types of radar systems, the focus of this report is the application of MIMO to airborne ground moving target indicator (GMTI) radar systems. In a GMTI system, a radar mounted on a moving airborne platform scans a region of the ground perpendicular to the aircraft's flight path with the goal of detecting moving targets. This is illustrated in Figure 1(a). Because the radar is illuminating the ground as well as the targets, a GMTI system must suppress the ground clutter while maintaining SNR on the targets. This is done by using the fact that stationary scatterers, such as ground clutter, lie on a collection of ridges (lines) in the angle-Doppler domain (assuming a uniform linear array with no crab). Moving targets will be displaced from the clutter ridge. This is illustrated in Figure 1(b). This angle-Doppler coupling can be exploited by adaptively designing two dimensional filters in the spatial (array) and temporal (pulse) domains that null out the clutter. This type of processing is known as space-time adpative processing (STAP) [14].

Note that the slower a target moves, the closer it will be to the clutter ridge. Thus it is important that the notch which nulls out the clutter is narrow so as to avoid masking slow moving targets. The ability to detect slowly moving targets is one primary metric for evaluating GMTI performance. Frequently, one refers to the minimum detectable velocity (MDV) of a GMTI system. Although it is possible to make a precise definition of what this means (though not a unique definition), we will be intentially be vague[1]. We will never quote specific values for MDV and instead use the term to refer to the general capability of a GMTI system to detect slowly moving targets. The second primary metric for evaluating GMTI performance is the accuracy with which a detected target can be geolocated. Equivalently, this is the accuracy with which the angle of arrival of the back-scattered target signal can be estimated.

[1] Our reluctance to be precise is due to the fact that most definitions of MDV do not directly relate to the actual operational performance of systems. Although many authors try to reduce the MDV to a single number, we suggest that at the very least, the MDV should be viewed as a function of the target RCS and range as one is certain to be able to detect a 10 dBsm target at 10 km at a lower velocity than a 0 dBsm target at 100 km. More generally, under a given set of operating conditions (aircraft crab, aircraft pitch, aircraft velocity, peak power, etc.), target parameters (RCS, range, etc.), detection criteria, and desired probability of detection ρ, there will be be some target radial velocity, below which a legitimate target will be detected with probability less than ρ because it falls into the null the system is putting around the clutter. We suggest there should be an MDV function which maps these parameters to this threshold velocity $MDV(\Theta)$, where Θ is a vector of these parameters.

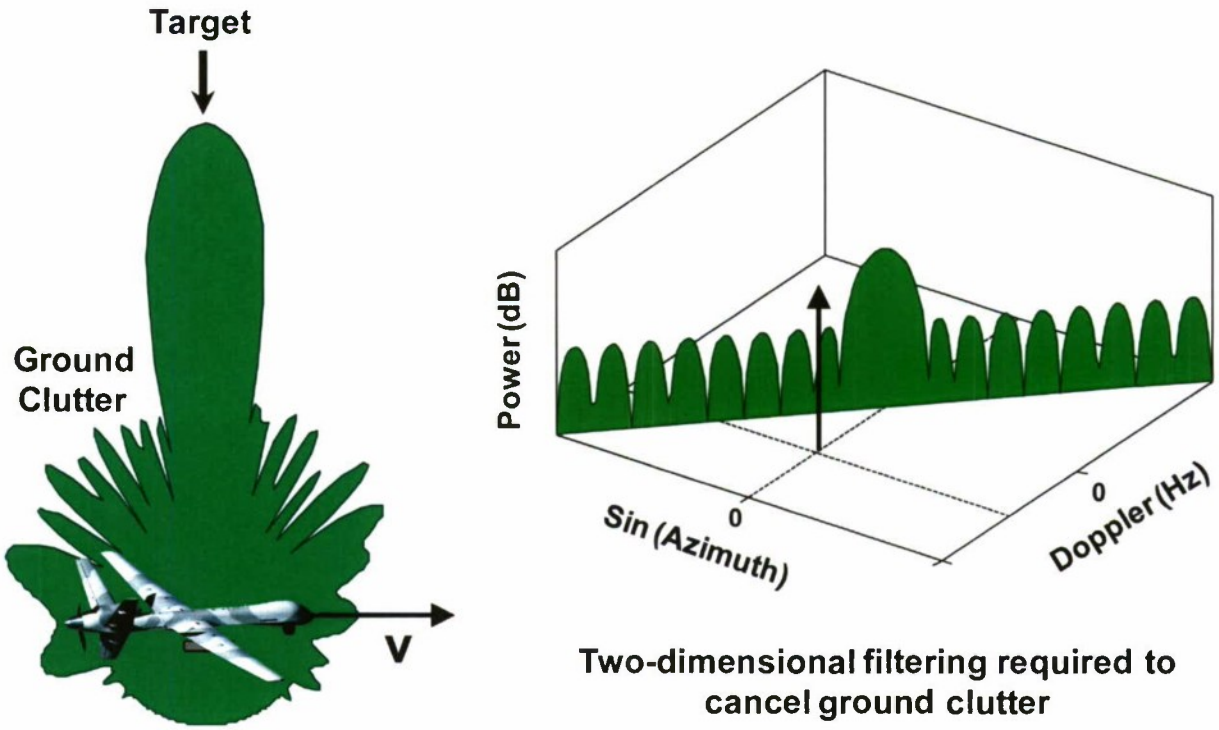

(a) Airborne GMTI system illuminating ground clutter and target.

(b) Ground clutter and target in angle-Doppler space.

Figure 1. Illustration of the idea behind GMTI radar.

In GMTI radar systems, the length of the array aperture has a strong effect on both the angle estimation accuracy and on the MDV. A longer array produces a narrower notch around the clutter thus lowering the MDV, and yields narrower beams for improved angle estimation performance.

As we will see, MIMO techniques offer the possibility of longer effective apertures and thus improved GMTI performance. The idea of applying MIMO to GMTI has been studied in the literature by way of simulations and theoretical analysis in [9], [8], [7], and [11] as well as others. In particular the article [8] has a very thorough exposition of the theoretical performance for MIMO systems. However, at this time there is no analysis of MIMO GMTI performance based on experimental data. This report is intended to fill this gap.

1.1 MIMO GMTI THEORY

We will now develop a mathematical framework in which to analyze some aspects of MIMO radar. Let n_T, n_R denote the number of transmitters and receivers, respectively. Let p index the pulse number. Let $s_i(p,t)$ be the signal transmitted by transmitter i on the p^{th} pulse where t parameterizes fast-time and $t = 0$ corresponds to the beginning of a pulse. Collect these into the vector of functions $\mathbf{s}(p,t) = [s_1(p,t), \ldots, s_{n_T}(p,t)]^T$. Similarly, the signals received at time t on the p^{th} pulse will be collected into the vector of functions $\mathbf{z}(p,t) = [z_1(p,t), \ldots, z_{n_R}(p,t)]^T$. The vectors

of functions $\mathbf{z}(p,t)$ and $\mathbf{s}(p,t)$ are related by

$$\mathbf{z}(p,t) = \int \mathbf{H}(p,r)\,\mathbf{s}(p,t-2r/c)\,dr + \mathbf{n}(p,t), \tag{1}$$

where r is slant range, $\mathbf{n}(p,t)$ is the noise, and $\mathbf{H}(p,r)$ is an $n_R \times n_T$ matrix of functions called the channel matrix. Here and throughout the paper, when the integrand of an integral is a matrix or vector, the integral applies to each component.

Let $\mathbf{x}_m$ and $\mathbf{y}_n$ be the coordinates of the transmitter and receiver phase centers. Then

$$\mathbf{a}_T(\mathbf{u}) = \left[e^{\frac{2\pi i}{\lambda}\mathbf{u}\cdot\mathbf{y}_1}, \ldots, e^{\frac{2\pi i}{\lambda}\mathbf{u}\cdot\mathbf{y}_{n_T}}\right]^T,$$

$$\mathbf{a}_R(\mathbf{u}) = \left[e^{\frac{2\pi i}{\lambda}\mathbf{u}\cdot\mathbf{x}_1}, \ldots, e^{\frac{2\pi i}{\lambda}\mathbf{u}\cdot\mathbf{x}_{n_R}}\right]^T$$

are the transmit and receive steering vectors for a narrowband signal at wavelength λ with $\mathbf{u}$ the unit vector pointing from the transmitters to the scatterer. The Doppler response for a stationary scatterer with unit direction vector $\mathbf{u}$, due to the platform velocity $\mathbf{v}_p$, will be

$$a_D(\mathbf{u},p) = \exp\left((p-1)\frac{4\pi i\mathbf{u}\cdot\mathbf{v}_p}{\lambda PRF}\right),$$

where PRF is pulse-repetition frequency of the system. In the case of a single stationary point scatterer at range r_0 (with unit direction vector $\mathbf{u}$), the channel matrix is given by

$$\mathbf{H}(p,r) \propto \delta(r-r_0)\,\mathbf{a}_R(\mathbf{u})\mathbf{a}_T(\mathbf{u})^T a_D(\mathbf{u},p), \tag{2}$$

where $\delta(r)$ is the Dirac delta function. The components of the channel matrix $\mathbf{H}(p,r)$ have the form

$$\mathbf{H}(p,r)_{nm} \propto \delta(r-r_0)\,e^{i\frac{2\pi}{\lambda}\mathbf{u}\cdot(\mathbf{y}_n+\mathbf{x}_m)}a_D(\mathbf{u},p). \tag{3}$$

The phase differences between the components of the channel matrix shown in (3) are identical to the phase differences between the elements of the steering vector for a SIMO array with $n_T n_R$ receiver phase centers located at positions $\mathbf{x}_m + \mathbf{y}_n$. This is how the MIMO virtual array arises. The waveforms of a MIMO system are chosen so that in each receive channel, it is possible to disentangle the scattering response of each of the n_T transmitted waveforms. The $n_T n_R$ separated channels will have the phase information of the full channel matrix, or equivalently of the full MIMO virtual array.

1.2 VIRTUAL ARRAY OPTIMIZATION

The virtual array can be thought of as the convolution of the transmit and receive arrays. It is easy to see that if the same array is used for transmitting and receiving, there will inevitably be multiple virtual array elements at the same locations in space. To make this explicit, suppose one has a one-dimensional uniform linear array with three phase centers at $\{-1,0,1\}$ (the coordinates

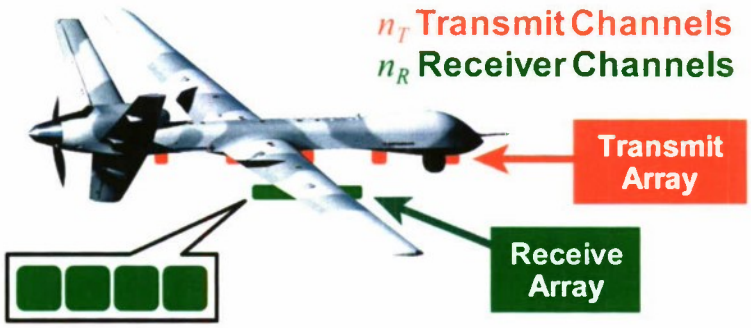

Figure 2. Notional sparse MIMO array on UAV.

being with respect to the line on which the array lies in units of half wavelengths). If this array is used in a MIMO fashion, it will produce a virtual array with phase centers at each of the points $\{-2, 2\}$, two phase centers at each of the points $\{-1, 1\}$ and three phase centers at 0. Note that the redundant phase centers can be interpreted as a triangular taper applied to the virtual aperture.

This suggests that to maximize the virtual array length, while maintaing a dense spacing of virtual array elements, one should use separate arrays for transmit and receive, one sparse and the other dense. Doing so it is possible to produce a long filled virtual array whose length is slightly larger than the sparse array but with the same element spacing as the dense array. This is illustrated in Figures 2 and 3. In the context of our previous toy example, consider transmitting out of an array with phase centers at $\{-1, 0, 1\}$ and receiving using an array with phase centers at $\{-4, -1, 2\}$. The resulting virtual array has one phase center at each of $\{-5, -4, -3, -2, -1, 0, 1, 2, 3\}$. While this examples uses the same number of phase centers as the previous toy example, the virtual array is made nearly twice as long by eliminating redundant phase centers[2].

Our view of the advantages of MIMO for GMTI is that MIMO allows the use of arrays that are long and physically sparse, but yield the performance of long filled virtual arrays. The benefits of a physically sparse array are the possibility of lighter arrays with few components, and flexibility to avoid airframe obstructions. Such arrays are good candidates for UAV GMTI systems. Sparse arrays with uniform element spacings are generally not usable if conventional processing is employed as they have severe grating lobe problems resulting in multiple blind speeds and ambiguous angle estimates. The MIMO approach allows the use of sparse physical arrays, by filling in the gaps with virtual array elements.

Although MIMO does have the potential to offer great performance improvements, it is important to ensure that one is making a fair comparison between a MIMO and SIMO system. Comparisons between MIMO and SIMO systems can be made by holding the energy and area rate

[2] Note that in many cases redundant phase centers may be desired for better fault tolerance. This could be accomodated by allowing either (or both) of the sparse and dense arrays to transmit and receive. One can also use geometries that are intermediate between sparse and dense arrays (for example, multiple widely separated dense arrays). However, as we will see in Section 2, the few sets of waveforms which we expect will have good GMTI performance do not easily lend themselves to supporting large numbers of transmitters. Thus one may have to make a trade between maximal virtual array length and redundancy.

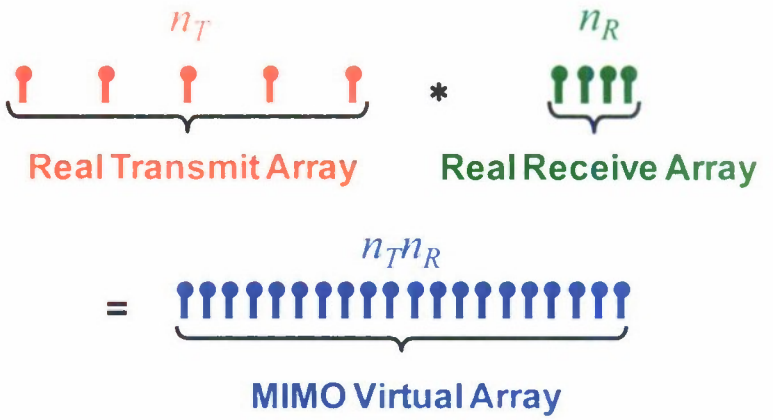

Figure 3. The virtual array is the convolution of the transmit and receive arrays.

(AR) of the systems constant as follows. Let P_{avg} be the average transmit power of a radar system, G_T be the transmit gain for a fully coherent transmit beam, and T be the coherent processing interval. Then for a SIMO system, the signal-to-noise ratio (SNR) and area rate have the following relationships (the omitted proportionality constants are the same for the MIMO and SIMO systems)

$$SNR_{SIMO} \propto P_{avg} G_T T \tag{4}$$

$$AR_{SIMO} \propto \frac{1}{G_T T}. \tag{5}$$

Next, consider a MIMO configuration of the same system where the phased array is partitioned into n_T subapertures. Maintaining the same total average transmit power for this system, the power can be distributed across the n_T subapertures resulting in an average module power of P_{avg}/n_T. The transmit subapertures have lower gain than the full aperture, so the MIMO transmit gain is G_T/n_T, a factor of n_T smaller than the SIMO case. However, the MIMO transmit beam covers an area n_T times broader than the SIMO transmit beam. Therefore, to match the SNR and area rate of the SIMO system, the MIMO integration time can be increased to $n_T T$

$$SNR_{MIMO} = SNR_{SIMO} \propto n_T \frac{P_{avg}}{n_T} \frac{G_T}{n_T} n_T T \tag{6}$$

$$AR_{MIMO} = AR_{SIMO} \propto \frac{1}{(G_T/n_T)(n_T T)}. \tag{7}$$

Note that since the SIMO system transmits narrow beams, it needs to scan over n_T angles to cover the same area that the MIMO system covers with a single transmit beam.

It is important to note that the assumption that the MIMO system can maintain SNR by integrating longer is not always valid. In certain situations it may be impossible to maintain target coherence for the full integration time the MIMO system would need to have equal SNR to some comparable SIMO system. This is likely to be more of an issue with faster targets. However, for our

primary interest in the use of MIMO GMTI in the detection of slowly moving targets, this should not be as much of an issue.

Another consideration when comparing the two systems is the array configuration. As we have mentioned, to achieve the longest virtual array, the MIMO receive array (or the MIMO transmit array) should be sparse, whereas a typical SIMO array uses densely packed elements to avoid grating lobes. However, if desired, one could construct a densely packed MIMO array or a sparse SIMO array. Although our primary consideration will be sparse MIMO configurations and dense SIMO configurations, in Section 7 we consider both dense and sparse configurations for the MIMO and SIMO systems.

1.3 CHANNEL ESTIMATION

Disentangling the transmitted waveforms in each receiver is equivalent to estimating the full channel matrix $\mathbf{H}(p,r)$ of (1). One approach is to match filter each receiver output with each transmitted waveform. The result of this match filtering operation is an estimate of the channel matrix[3], denoted $\widehat{\mathbf{H}}(p,r)$,

$$\begin{aligned}\widehat{\mathbf{H}}(p,r) &= \int \mathbf{z}(p,t)\,\mathbf{s}(p,t-2r/c)^H\,dt \\ &= \int\int \mathbf{H}(p,u)\,\mathbf{s}(p,t-2u/c)\,\mathbf{s}(p,t-2r/c)^H\,du\,dt + \widehat{\mathbf{n}}(p,r) \\ &= \int \mathbf{H}(p,u)\,\mathbf{C}(p,2(u-r)/c)\,du + \widehat{\mathbf{n}}(p,r), \end{aligned} \tag{8}$$

where

$$\mathbf{C}(p,t) = \int \mathbf{s}(p,\tau)\,\mathbf{s}(p,\tau+t)^H\,d\tau$$

is the waveform cross-correlation, $\widehat{\mathbf{n}}(p,r)$ denotes the noise after applying the matched filter, and superscript H denotes the conjugate transpose.

Let $f_n = 2\pi\frac{n}{N_p}$, $n = 0,\ldots,N_p-1$, where N_p is the number of pulses per CPI. Let $\underline{\mathbf{H}}(f_n,r)$, $\underline{\mathbf{C}}(f_n,r)$ be the DFT of $\mathbf{H}$ and $\mathbf{C}$ in the pulse variable. It will be useful to observe that the DFT of (8) in the pulse variable is

$$\underline{\widehat{\mathbf{H}}}(f_n,r) = \int \sum_{m=1}^{N_p} \underline{\mathbf{H}}(f_m,u)\,\underline{\mathbf{C}}(f_{n-m},2(u-r)/c)\,du, \tag{9}$$

where by abuse of notation we let $f_{n-m} = f_{N_p-(n-m)}$ for $n-m<0$, and where we have omitted the noise term. Observe that if there is a single point scatterer with Doppler frequency f_{n_0} at range

[3] Whether or not this is a good estimate depends on the waveforms used, in particular on $\mathbf{C}(p,t)$.

r_0, then $\underline{\mathbf{H}}(f_n, r) = \delta_{f_{n_0}}(f_n)\,\delta(r - r_0)\,\mathbf{A}$ where $\mathbf{A} = \mathbf{a}_R(\mathbf{u})\mathbf{a}_T(\mathbf{u})^T$ and $\delta_{f_{n_0}}$ is a discrete point mass at the frequency f_{n_0}.

To accurately recover $\mathbf{A}$, we desire that $\underline{\mathbf{C}}(f_n, r)$ is as close as possible to $\delta_0(f_n)\,\delta(r)\,\mathbf{I}$. This is of course impossible to satisfy exactly, however, one might hope that it would be possible to have

$$\underline{\mathbf{C}}(f_n, r) = \delta_0(f_n)\,\sigma(r)\,\mathbf{I}$$

for some scalar auto-correlation function $\sigma(r)$. This too is impossible unless the waveforms vanish identically. To see this, first note that if the cross-correlation completely localizes in Doppler, then the transmitted waveforms do not vary from pulse to pulse. Next, if a pair of waveforms has zero cross-correlation at all delays, then for all t

$$0 = \int s_i(\tau)\,s_j(\tau + t)^*\,d\tau = \int \underline{s}_i(f)\,\underline{s}_j(f)^* e^{-2\pi i f t}\,df, \tag{10}$$

here the Fourier transform indicated by the underline is in fast time and we have omitted the pulse index to work in a single pulse; the $*$ indicates conjugation. Equation (10) implies $\underline{s}_i(f)$ and $\underline{s}_j(f)$ have disjoint supports. On the other hand the requirement to have identical auto-correlation functions implies $|\underline{s}_i(f)|^2$ and $|\underline{s}_j(f)|^2$ are identical. This can only be satisfied if the waveforms vanish.

This implies that the waveforms have nonzero cross-correlation and/or they have mismatched auto-correlation functions. In the next section we will discuss the impact of the waveform cross-correlation and auto-correlation on MIMO GMTI performance.

This page intentionally left blank.

2. WAVEFORM CONSIDERATIONS

As we mentioned in the introduction, a GMTI system employing STAP suppresses clutter by adaptively constructing filters in the spatial (array) and temporal (pulse) domains to null the clutter without suppressing the targets. For STAP, the rank of the clutter covariance matrix corresponds to the number of degrees of freedom needed to cancel the clutter. As we will see, without careful choice of waveforms for MIMO systems, there will be an inevitable increase in the rank of the clutter covariance, and thus a decrease in overall performance. A very elegant and thorough analysis of this phenomenon is contained in [13]. In this chapter, we will give a concise summary employing a similar analysis.

Before starting the analysis, let us give a heuristic explanation for this increase in rank. Recall from Section 1.3 that an ideal MIMO waveform would have an autocorrelation function satisfying

$$\underline{\mathbf{C}}(f_n, r) = \delta_0(f_n)\sigma(r)\mathbf{I},$$

which we noted was impossible. If one considers the integral in (8), one sees that inevitable differences between the entries of $\mathbf{C}(p, r)$ will cause the clutter to be smeared out differently in different channels. This causes the clutter to decorrelate and is the source of the increased rank. With care it can be avoided in certain situations.

2.1 CLUTTER COVARIANCE MATRIX RANK

Most discussions about clutter rank, in particular the well known Brennan rule, are with respect to the full $MN_p \times MN_p$ space-time covariance matrix where N_p is the number of pulses and M the number of spatial degrees of freedom. We will instead focus on the spatial array covariance in a single Doppler bin which is only an $M \times M$ matrix. In the MIMO case $M = n_R n_T$ and in the SIMO case $M = n_R$. Note that for a SIMO array for which all the clutter at a given Doppler is at the same angle, the spatial covariance matrix of the samples in that Doppler bin should effectively be rank 1, with the dominant eigenvector being the steering vector. It would be desirable to have the same outcome with the MIMO array, requiring only one degree of freedom to cancel the clutter.

Let us now consider a MIMO array. For simplicity, let us assume our transmit and receive arrays are uniform linear arrays, with d_T, d_R the transmit and receive element spacings. Then

$$\mathbf{a}_R(\theta) = [1, e^{\frac{2\pi i}{\lambda} d_R \sin(\theta)}, \ldots, e^{\frac{2\pi i}{\lambda} n_R d_R \sin(\theta)}]^T$$

$$\mathbf{a}_T(\theta) = [1, e^{\frac{2\pi i}{\lambda} d_T \sin(\theta)}, \ldots, e^{\frac{2\pi i}{\lambda} n_T d_T \sin(\theta)}]^T$$

are the transmit and receive steering vectors for a scatterer at angle θ (where this angle is the off-broadside angle or equivalently the complement of the cone angle). Clutter at angle θ will have a normalized Doppler of $2\pi\alpha \sin(\theta)$, where $\alpha = \frac{2v_p}{\lambda PRF}$, and v_p is the platform speed. Thus

$$a_D(\theta, p) = \exp\left(2\pi i \left(p - 1\right) \alpha \sin(\theta)\right), \qquad p = 1, \ldots, N_p \tag{11}$$

is the Doppler response for a scatterer at angle θ.

We model ground clutter as the result of scattering off a dense collection of point scatterers. As in (2) (but now written with respect to angle), the channel matrix for a single point scatterer at angle θ and range u is

$$\mathbf{H}_{\theta,u}(p,r) = \delta(r-u)g_\theta(u)\,\mathbf{a}_R(\theta)\mathbf{a}_T(\theta)^T a_D(\theta,p),$$

where $g_\theta(u)$ is the complex scattering coefficient. Then since we assume a dense collections of scatterers we can obtain the channel matrix by integrating in range and angle,

$$\mathbf{H}(p,r) = \int\int \mathbf{H}_{\theta,u}(p,r)dud\theta = \int g_\theta(r)\,\mathbf{a}_R(\theta)\mathbf{a}_T(\theta)^T a_D(\theta,p)d\theta.$$

Let $h_\theta(n)$ be the amplitude at frequency f_n of $a_D(\theta,p)$ obtained from the DFT in the pulse variable. The function $h_\theta(n)$ can be written explicitly as

$$h_\theta(n) = \exp\left(-\pi i(N_p-1)\left(\frac{n}{N_p} - \alpha\sin(\theta)\right)\right)D(\theta,N_p,n),$$

for

$$D(\theta,N_p,n) = \frac{\sin(\pi(n - N_p\alpha\sin(\theta)))}{\sin\left(\pi\left(\frac{n}{N_p} - \alpha\sin(\theta)\right)\right)}. \tag{12}$$

Thus

$$\underline{\mathbf{H}}(f_n,r) = \int g_\theta(r)\,h_\theta(n)\,\mathbf{a}_R(\theta)\,\mathbf{a}_T(\theta)^T\,d\theta. \tag{13}$$

Note that for $\frac{n}{N_p} - \alpha\sin(\theta)$ close to 0, we can apply the linear approximation $\sin(x) \approx x$ to the denominator of (12) to obtain the approximation

$$D(\theta,N_p,n) \approx N_p\,\mathrm{sinc}\left(N_P\left(\frac{n}{N_p} - \alpha\sin(\theta)\right)\right).$$

Then since $\lim_{a\to 0}\frac{1}{a}\mathrm{sinc}(x/a) \to \delta(x)$, we see that for large N_p it is reasonable to approximate the integral in (13) by

$$\underline{\mathbf{H}}(f_n,r) \approx g_n(r)\mathbf{a}_R(\theta_n)\mathbf{a}_T(\theta_n)^T, \tag{14}$$

where θ_n is the angle corresponding to Doppler frequency $f_n = 2\pi\frac{n}{N_p}$, and $g_n(r) = g_{\theta_n}(r)$. For simplicity, we assume that the element spacings and platform velocity are such that for each Doppler frequency f_n, there is a unique angle θ_n at which clutter has this Doppler frequency.

Let *vec* denote the operator which stacks the columns of a matrix as a vector. Note that

$$\mathbf{v}_n(r) = vec(\widehat{\underline{\mathbf{H}}}(f_n,r))$$

is our estimate of the virtual array response to scatterers along the clutter ray corresponding to Doppler frequency f_n. Substituting (14) into (9) and ignoring the noise term, one can write

$$\mathbf{v}_n(r) = \sum_{m=1}^{N_p} \int g_m(u) \left(\mathbf{a}_R(\theta_m) \otimes \mathbf{I}_{n_T}\right) \underline{\mathbf{C}}(f_{n-m}, 2(u-r)/c)^T \, \mathbf{a}_T(\theta_m) \, du.$$

The virtual array covariance matrix is $E[\mathbf{v}_n(r)\mathbf{v}_n(r)^H]$, where the expectation is over clutter realizations. Let us assume that $E[g_l(r)g_m(s)^*] = p_l(r)\delta_{lm}\delta(r-s)$, where δ_{lm} is the Kronecker delta. Here, p_l are functions that encode the reflected clutter power, and we are assuming the clutter is uncorrelated in adjacent Doppler bins. Then one can compute that

$$E[\mathbf{v}_n(r)\mathbf{v}_n(r)^H] = \sum_{l=1}^{N_p} (\mathbf{a}_R(\theta_l) \otimes \mathbf{I}_{n_T}) \mathbf{G}_{ln}(r, \theta_l) (\mathbf{a}_R(\theta_l) \otimes \mathbf{I}_{n_T})^H \tag{15}$$

where

$$\mathbf{G}_{ln}(r, \theta_l) = \int p_l(u) \underline{\mathbf{C}}^T(f_{n-l}, 2(u-r)/c) \mathbf{a}_T(\theta_l) \mathbf{a}_T^H(\theta_l) \underline{\mathbf{C}}^*(f_{n-l}, 2(u-r)/c) du, \tag{16}$$

and where the $*$ indicates conjugation (but not conjugate transpose). We call $\mathbf{G}_{ln}$ the integrated waveform cross-correlation matrix. Note that $\mathbf{G}_{ln}$ is a matrix for each choice of indices l,n. From this equation, one can see that the structure of $\underline{\mathbf{C}}(f_l, t)$ will directly influence the rank of the clutter covariance matrix.

Suppose that the sum in (15) has a single nonzero term (say corresponding to $l = n$) so that

$$E[\mathbf{v}_n(r)\mathbf{v}_n(r)^H] = (\mathbf{a}_R(\theta_n) \otimes \mathbf{I}_{n_T}) \mathbf{G}_{nn}(r, \theta_n) (\mathbf{a}_R(\theta_n) \otimes \mathbf{I}_{n_T})^H. \tag{17}$$

Observe that the columns of $\frac{1}{\sqrt{n_R}}(\mathbf{a}_R(\theta_n) \otimes \mathbf{I}_{n_T})$ are orthonormal. If

$$\mathbf{G}_{nn}(r, \theta_n) = \mathbf{F}(r, \theta_n) \mathbf{\Lambda}(r, \theta_n) \mathbf{F}(r, \theta_n)^H$$

is an eigendecomposition of $\mathbf{G}_{nn}(r, \theta_n)$ (here $\mathbf{F}(r, \theta_n)$ is orthonormal and $\mathbf{\Lambda}(r, \theta_n)$ is diagonal), then (17) can be written

$$\mathbf{E}(\theta_n)(n_R \mathbf{\Lambda}(r, \theta_n)) \mathbf{E}(\theta_n)^H,$$

where

$$\mathbf{E}(\theta_n) = \left((\mathbf{a}_R(\theta_n) \otimes \mathbf{I}_{n_T}) \mathbf{F}(r, \theta_n) \frac{1}{\sqrt{n_R}} \right).$$

In particular, (17) has $n_R n_T - n_T$ eigenvalues of 0, and n_T eigenvalues n_R times larger than those of $\mathbf{G}_{nn}(r, \theta_n)$. In this case, note that if $\underline{\mathbf{C}}(f_0, t) = \sigma(t)\, \mathbf{B}$ for some constant matrix $\mathbf{B}$ and some scalar function $\sigma(t)$, then

$$\mathbf{G}_{nn}(r, \theta_n) = \left(\int p_n(u) \, |\sigma(2(u-r)/c)|^2 du \right) \mathbf{B}^T \mathbf{a}_T(\theta_n) \mathbf{a}_T^H(\theta_n) \mathbf{B}^*. \tag{18}$$

Since $\mathbf{a}_T(\theta_n)\mathbf{a}_T^H(\theta_n)$ is rank-1, (18) is as well and thus so is the clutter covariance.

On the other hand, consider a waveform set in which the waveforms $\mathbf{s}(t)$ are orthogonal at all delays and the same waveforms are repeated from pulse to pulse. In this case, we again only need to consider $\mathbf{G}_{nn}$. Note that

$$\underline{\mathbf{C}}(f_0,t)_{ij} \propto \int s_i(\tau)\, s_j(\tau+t)^*\, d\tau = \int \underline{s}_i(f)\, \underline{s}_j(f)^*\, e^{-2\pi i f t}\, df,$$

which is 0 for $i \neq j$. Assume that the clutter power $p_l(u) = 1$ for simplicity. Then by Parseval's theorem

$$\mathbf{G}_{nn}(r,\theta_n) = \int \underline{\mathbf{C}}^T(f_0, 2(u-r)/c)\, \mathbf{a}_T(\theta_n)\, \mathbf{a}_T^H(\theta_n)\, \underline{\mathbf{C}}^*(f_0, 2(u-r)/c)\, du$$

$$= \frac{c}{2} \sum_{j=1}^{n_T} \left(\int_{\Omega_j} |\mathbf{a}_T(\theta_n)_j|^2 |\underline{s}_j(f)|^4 df \right) \mathbf{e}_j \mathbf{e}_j^H,$$

where $\mathbf{e}_j$ is the vector with a one in the j^{th} component and zeros elsewhere, and Ω_j is the support of $\underline{s}_j(f)$. Consequently, $\mathbf{G}_{nn}$ and thus the clutter covariance will be rank n_T for waveforms that achieve orthogonality in fast time.

Essentially, for fast-time MIMO waveforms, although our MIMO processing has given us n_T times more degrees of freedom, we have to expend all of them to suppress the clutter which now occupies a subspace n_T times larger. Thus, we will not gain any improvement in performance. The increased clutter rank, it turns out, depends crucially on the assumption that clutter fills range and Doppler (i.e., that $p_l(u)$ was nonzero for all l and $u > 0$). If the clutter is limited in range or Doppler, it is possible to choose orthogonal waveforms so that the clutter covariance has rank one. In the next section, we describe two classes of waveforms that achieve rank one clutter covariance under certain restrictions.

3. LOW CLUTTER RANK MIMO WAVEFORMS

First, consider time division multiple access (TDMA) waveforms. These waveforms are intuitively very simple, we only let one transmitter transmit at a time as illustrated in Figure 4. As we previously noted, the clutter covariance matrix will have rank 1 if the sum in (15) has the single term, say for $l = n$, and $\underline{\mathbf{C}}(f_0, 2(u-r)/c) = \sigma(2(u-r)/c)\,\mathbf{B}$ for a scalar function σ and constant matrix $\mathbf{B}$. Suppose $\forall i$, $g_i(r) = 0$ for $r > R$ so that clutter has finite extent in range. Then the integral in (16) will only extend from 0 to R. Choose a fixed waveform $s(t)$ and have transmitter m transmit a copy of this waveform delayed by $2(m-1)R/c + \tau$, $m = 1, \ldots, n_T$ where τ is the pulse width. It is easy to see that for $0 < t < 2R/c$, $\mathbf{C}(p,t) = \sigma(t)\mathbf{I}$, where σ is the autocorrelation function of s. For $t > 2R/c$ this relationship breaks down, but since the integral in (16) does not extend past $2R/c$, the clutter covariance will have rank 1.

Next, consider Doppler division multiple access (DDMA) waveforms. These have been proposed as candidate MIMO waveforms in [12], and their potential for maintaining low clutter rank is discussed in [9]. These waveforms achieve orthogonality using slow time. The idea is that each transmitter emits a Doppler modulated pulse train in such a way that the responses to each transmitter are separated in Doppler. This is illustrated in Figure 5. Let us assume that the clutter occupies a finite extent in Doppler so that $g_i(r) = 0$ for f_i outside of the band $[\frac{-2\pi}{2n_T}, \frac{2\pi}{2n_T}]$. Again, choose a fixed waveform, $s(t)$. The collection of MIMO waveforms are defined by having each transmitter emit Doppler-shifted copies of s, meaning, on the p^{th} pulse, transmitter m will transmit $e^{ip(m-1)\psi}s(t)$, $m = 1, \ldots, n_T$ for $\psi = \frac{2\pi}{n_T}$. In this case, one finds that $\underline{\mathbf{C}}(f_i, t) = \delta_0(f_i)\,\sigma(t)\,\mathbf{I} + \mathbf{D}(f_i)$, where σ is the autocorrelation function of s and $\mathbf{D}(f_i)$ are Doppler ambiguous terms which are nonzero only for f_i outside the band $[\frac{-2\pi}{n_T}, \frac{2\pi}{n_T}]$. Thus for $f_n \in [\frac{-2\pi}{2n_T}, \frac{2\pi}{2n_T}]$, the sum in (15) again reduces to simply

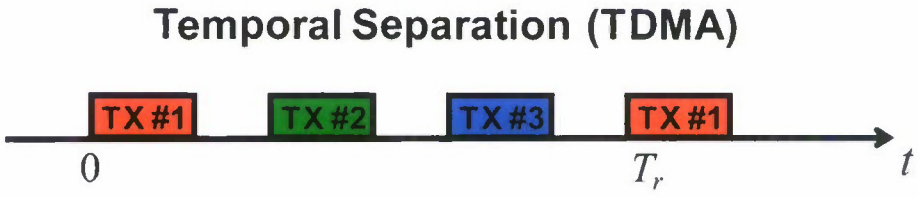

Figure 4. Illustration of TDMA waveforms.

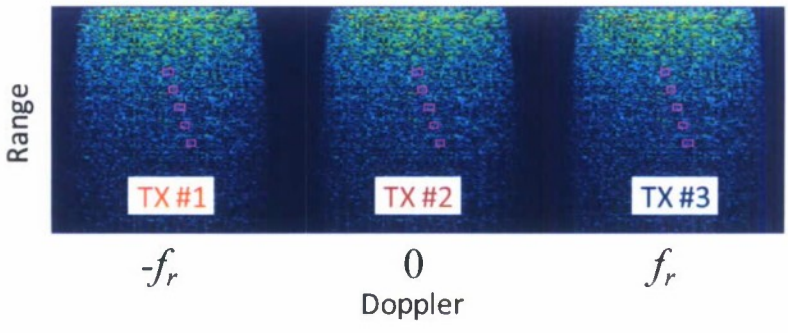

Figure 5. Illustration of radar response from DDMA waveforms.

a single term, and it can be seen that the clutter covariance matrix has rank 1. Also, from the form of $\underline{\mathbf{C}}(f_n, t)$, even though the waveforms are multiples of each other on each pulse, because of the Doppler modulation, we can easily extract the channel.

3.1 WAVEFORM CONSTRAINTS

The number of realizable DDMA or TDMA transmit channels is constrained by the pulse repetition frequency (PRF) of the system as well as the clutter bandwidth. DDMA and TDMA waveforms are well-suited to systems that operate at short to mid-range since these systems can tolerate relatively high PRFs without range ambiguities.

Although the assumptions that clutter is limited in range or Doppler used in our analysis of DDMA and TDMA waveforms will never be realized exactly in real life, they should hold approximately in many cases. In particular, for a good antenna pattern with low sidelobes, clutter will effectively have a finite extent in Doppler. Similarly, the R^{-4} fall off in power as a function of range means that clutter will also effectively be limited in range.

Of course large discretes in sidelobes or at long ranges can still create problems. In actual practice, because of noise and other effects, the covariance matrix will always be full rank. Instead, one is interested in what extent different waveforms may increase the number of eigenvalues that are above the noise floor.

We will now present some examples of simulated and experimental data illustrating this increase in clutter covariance rank and the fact that the DDMA waveforms do not suffer from this increase in rank.

3.2 SIMULATED CLUTTER DATA

To investigate the MIMO clutter covariance matrices for different waveforms, a simulation was developed that used a sandpaper earth approximation for ground clutter and that included a variety of realistic effects. In this paper, we compare two waveforms. First, for a simple (naïve) example of a set of nearly orthogonal waveforms, we will consider a set of waveforms of constant modulus where for each fast-time sample the phase is drawn from a uniform distribution. We can ensure that the n_T waveforms are orthogonal (at 0 delay) by taking the SVD of the initial set of random samples. Though random in fast time, the same waveforms will be repeated in slow time. We will compare the clutter eigenvalue distribution of this random waveform and of the DDMA waveforms described earlier. For the simulation, we use $n_T = 4$ transmitters.

In **Figure** 6, we show the eigenvalues in a single Doppler bin for the random and DDMA waveforms in the case in which there are four transmitters and four receivers. As expected, for the random waveform at least four eigenvalues are well above the noise floor. A variety of other possible waveforms also display this increased clutter covariance matrix rank. Observe that for the DDMA waveform the matrix has a single dominant eigenvector.

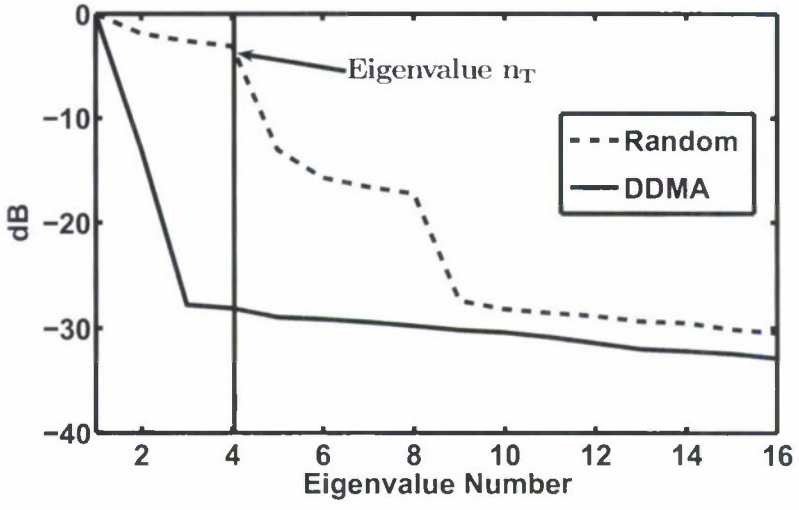

Figure 6. Peak normalized eigenvalues of spatial array covariance matrix in one Doppler bin for simulated data using random and DDMA waveforms.

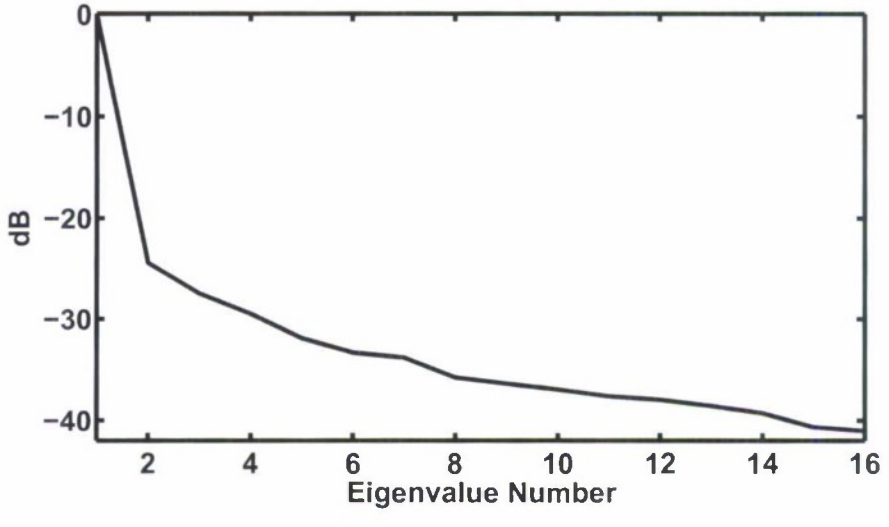

Figure 7. Peak normalized experimental eigenvalues of the spatial array covariance matrix in one Doppler bin for DDMA waveforms.

3.3 EXPERIMENTAL CLUTTER DATA

In **Figure** 7, we present the eigenvalues in a single Doppler bin for the experimental data (which is the subject of the rest of this report) that uses the DDMA waveforms. The system

parameters are presented in Section 4. Observe that the shape of the experimental DDMA clutter eigenvalue distribution agrees well with the simulated eigenvalues and, in particular, also has a single dominant eigenvector.

3.4 FINAL THOUGHTS ON WAVEFORMS

As we have tried to illustrate, although in principle a MIMO system has much freedom regarding the multiple transmitted waveforms, for GMTI applications, there are substantial constraints imposed by the requirement to maintain low clutter rank. Any application of MIMO to GMTI must ensure that the waveforms will not degrade performance unnecessarily. At the current time, we recommend the use of DDMA or TDMA waveforms for MIMO GMTI. They are simple to process and have good properties for GMTI as we have indicated. Their primary disadvantage is the required high PRF.

4. AIRBORNE EXPERIMENT

A Twin Otter aircraft was selected as the platform for a small-scale MIMO radar experiment. The MIMO radar testbed operates at S-band with up to 6 independent transmit channels and 8 independent receive channels. The operator can manually activate or deactivate each channel to configure the number and relative placement of transmitters and receivers in the MIMO array. Table 1 summarizes some of the important testbed parameters, and a photograph of the testbed is shown in Figure 8. The frequency and bandwidth of the system were chosen due to availability of existing hardware and low-cost commercial components. GMTI data was collected on instrumented targets with both sparse and dense SIMO and MIMO configurations during a two-day experiment at Ft Devens, Massachusetts. Ground activity for the experiment included instrumented civilian vehicles with a diversity of ground speeds and aspect angles.

The MIMO array was mounted on the port side of the Twin Otter with a 30 degree depression angle. It is composed of two rows of 13 commercial patch antennas as shown in Figure 9, where the patches have a 30 degree beamwidth and are uniformly spaced horizontally with an interelement

Figure 8. MIMO flat panel array mounted on the side of the Twin Otter aircraft.

TABLE 1
Experimental Radar System Parameters

Center Frequency	2.37 GHz
Bandwidth	10 MHz
Pulse Width	12 μsec
PRF	6667 Hz
Peak Element[a] Power	25 W
Element Gain	13 dBi
Element Beamwidth	30 deg
Altitude	3 km
Air Speed	70 m/s
Range to Aimpoint	5 km

[a] An element is a single patch antenna on the array.

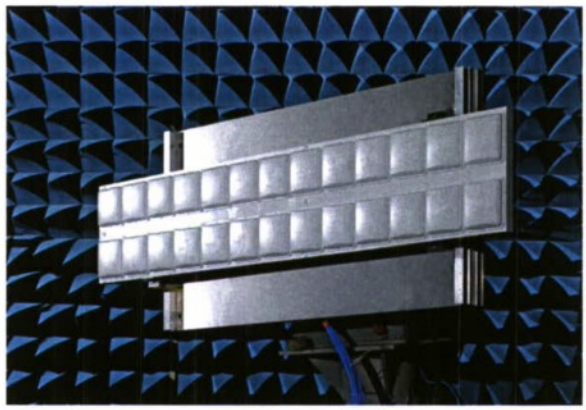

Figure 9. MIMO testbed array with a grid of 13 patch antennas across and 2 down in test chamber.

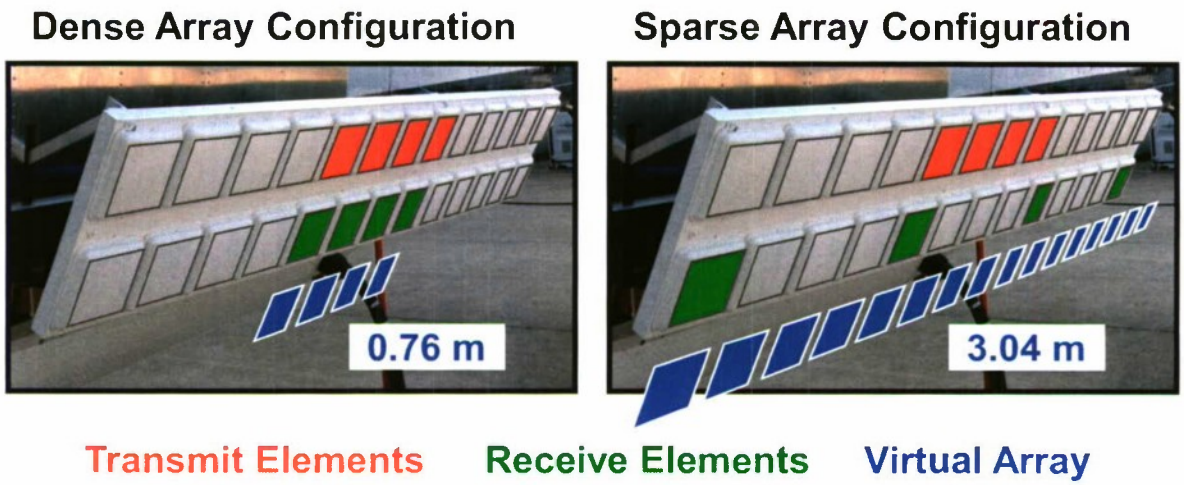

Figure 10. MIMO testbed array with subarrays for different modes highlighted.

spacing of 19 cm. To configure the MIMO array, up to 6 patches on the upper row are manually connected to independent transmit channels and up to 8 patches on the lower row are manually connected to the available receive channels. For the results presented here, we focus on the case of $n_T = 4$ transmit modules and $n_R = 4$ receive modules, where the receive array spacing has been evaluated in both densely packed and sparse configurations. The nominal dense SIMO and sparse MIMO array configurations are shown in Figure 10. The results presented in Section 6 are based on these nominal configurations. Section 7 further explores array configurations by examining a SIMO system with the sparse receive array shown in Figure 10 and a MIMO system with the dense receive array of Figure 10 (these configurations have virtual arrays different from what is pictured). The effective apertures for these four cases are given in Table 2.

TABLE 2
Effective Aperture Lengths for SIMO and MIMO Configurations

Array Configuration	Effective Aperture (m)
Dense SIMO	0.76
Dense MIMO	1.33
Sparse SIMO	2.47
Sparse MIMO	3.04

The testbed design allows arbitrary waveforms to be independently programmed for each transmit channel. In this experiment, we collected data using the Doppler-division multiple access (DDMA) waveforms and the Time-division multiple access (TDMA) waveforms described in Section 3. Both of these waveforms are based on a standard linear FM chirp to achieve low range and Doppler sidelobes. Recall that the DDMA waveform set is constructed by applying slow time phase ramps to the LFM pulse train, thus modulating the chirp to different regions of the Doppler space so that the clutter responses of the transmitters do not overlap. The TDMA waveforms simply amount to having one transmitter transmitting at a time. We also collected data for a slow time phase coded waveform set, where each transmitter transmits an LFM pulse but with randomly varying phase from pulse to pulse. These random phase waveforms require a somewhat more involved processing chain than the DDMA/TDMA waveforms which we will describe in a separate report.

For comparison purposes, conventional SIMO operation of the testbed is also considered. In fact, depending on the processing techniques applied to the data, the DDMA MIMO collection can also be interpreted as a SIMO collection with four scan angles interleaved on a pulse-to-pulse basis. The reason for this is that the DDMA waveforms were implemented by applying phase ramps across the transmit array that effectively sweep a coherent transmit beam through four angles from pulse to pulse. That is, during pulses $1, 5, 9, \ldots$, a beam is formed in the direction of angle 1; during pulses $2, 6, 10, \ldots$, a beam is formed in the direction of angle 2; and so forth. The beampatterns formed by the DDMA waveforms on pulses $1, 2, 3$, and 4 are plotted in Figure 11. Thus by taking every n_T^{th} pulse and processing this subset of pulses as a coherent processing interval (CPI), we treat the data as a SIMO collection with a pulse repetition interval (PRI) that is n_T times longer than the system PRI. This approach meets the equal energy and area rate requirement laid out in Section 1, but the balance in SNR for SIMO and MIMO is achieved by making trades at the PRI level rather than the CPI level. For this experiment, a MIMO CPI consists of 720 pulses with a 150 μsec PRI for a total length of 101 msec. The data viewed as SIMO system is composed of four 180-pulse CPIs (interleaved on a pulse by pulse basis), with each CPI also of length 101 msec, but the effective PRI is 600 μsec. Note that these SIMO and MIMO setups operate on the same data, but are simply processed in different fashions.

We also collected data where the array was operated in a more traditional SIMO mode, in which four CPIs of 180 pulses each scan through four look angles sequentially. The PRI is 150 μsec, and since the CPIs are not interleaved as they are in the DDMA data, the PRI is actually 150 μsec. Thus for this conventional data, the Doppler resolution is $1/4^{th}$ of that of the DDMA data treated as MIMO or SIMO. To distinguish between the two types of SIMO data, we will refer to

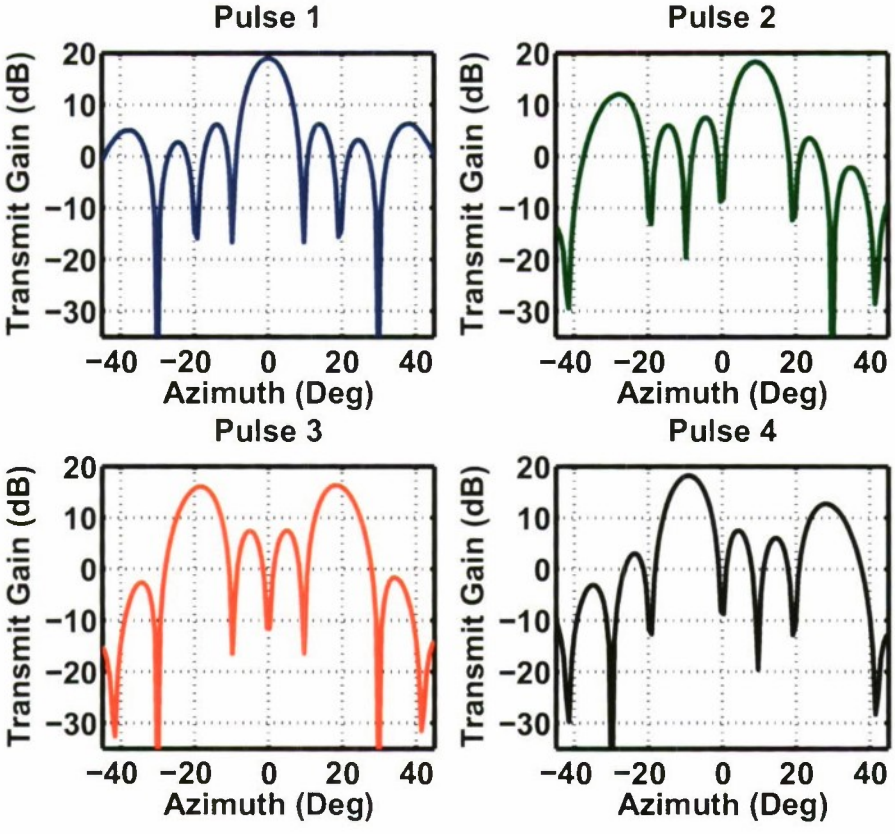

Figure 11. The beam patterns formed on successive pulses by the slow time phase ramp of the DDMA waveforms.

the DDMA data processed in a SIMO fashion as DDMA SIMO data, and refer to the traditional lower resolution SIMO data as the conventional SIMO data. This conventional SIMO data was interleaved with the MIMO data, so is collected essentially simultaneously, as each DDMA dwell is followed 101 msec later by four conventional SIMO CPIs of the form just described.

5. SIGNAL PROCESSING

Let us now describe the processing chain used for the experimental MIMO radar data. A block diagram of the processing chain is show in Figure 12.

Figure 12. Signal processing chain block diagram.

The first step is to match filter the raw I/Q data from each receiver with the transmitted waveforms, yielding $n_T n_R$ range-pulse images. We move to the range-Doppler domain using a windowed FFT. The windowing suppresses Doppler sidelobes to reduce interference between adjacent DDMA channels. An example range-Doppler map following the matched filter and FFT is shown in Figure 13. Because we are using DDMA waveforms, there are effectively four range-Doppler maps appearing in this image. The virtual array output for the transmit/receive pair under consideration is the center "stripe" of this range-Doppler map corresponding to frequencies in the interval $[\frac{-PRF}{2n_T}, \frac{PRF}{2n_T}]$. Thus for each of the $n_T n_R$ range-Doppler images we extract a single sub-chip, corresponding to this Doppler interval. An inverse FFT yields $n_T n_R$ range-(pseudo) pulse images, which are the outputs of our virtual array. Note that before extracting the virtual array subchip, the MIMO system had 720 pulses per CPI with a 150 μsec PRI. After extracting the virtual array, the range-(pseudo) pulse images have only 180 pulses per CPI, but the effective PRI is 600 μsec just like the DDMA SIMO data.

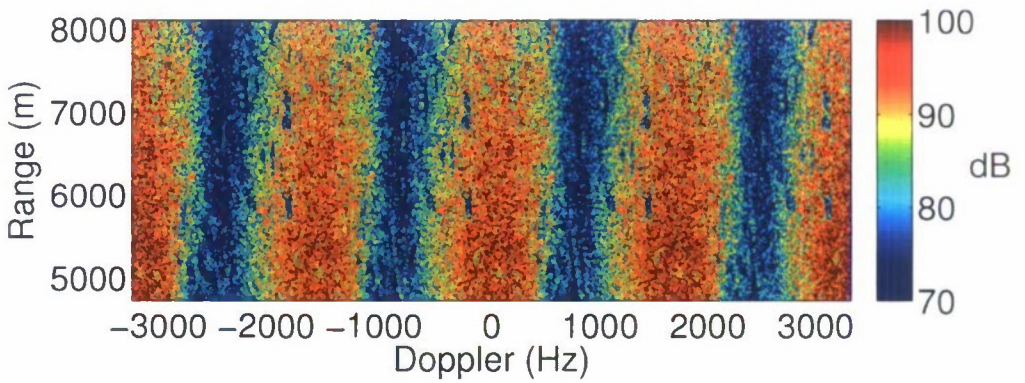

Figure 13. DDMA MIMO data after a matched filter and Doppler processing.

5.1 MIMO CHANNEL EQUALIZATION

We will now describe the calibration procedure. Unfortunately, there was no end-to-end system characterization done prior to the data collection due to time constraints. Additionally, there were no ground targets that were visible pre-STAP with known location that could be used for calibration (we had corner reflectors on the ground but they did not appear in the data). Consequently, we were forced to develop a data adaptive calibration approach.

Let us first outline our equalization approach. Consider a uniform linear array and suppose the platform velocity is such that from pulse to pulse each array element moves to the position its neighbor was at on the previous pulse. Then, if we shift the data from different array elements in the pulse domain by integer amounts in the correct fashion (ignoring the edges), after shifting, the data from each array element will have been recorded at the same physical location in space (but at different times). Thus any stationary target perceived by the array should produce identical outputs for all elements. This idea is used in the DPCA clutter cancellation technique. We can instead use it to calibrate the array by designing filters that make the response of the shifted array elements to a stationary target as similar as possible. In practice the array will not move by an integer element shift from pulse to pulse, but we can still use this idea, it will simply require shifting by a fractional number of pulses. The stationary target we will use is the ground clutter. Now let us examine the details more explicitly.

Consider a uniform linear array under ideal conditions with no crab. Assume the aircraft velocity is v, the wavelength is λ, the interelement spacing is d, and the PRI length is T_{PRI}. First, we need to shift our data in the pulse domain so that the clutter in all the virtual array elements is aligned coherently. Shifting the data from the n^{th} virtual array channel by $\frac{-nd}{2vT_{PRI}}$ pulses will have the desired effect of making the clutter signal in each virtual array channel identical. This shift factor can be derived through a displaced-phase-center antenna (DPCA) type analysis.

More precisely, consider a clutter patch at an azimuthal angle of θ_c and elevation angle of ϕ_c appearing at a Doppler frequency of f_c. For a uniform linear array, define the normalized spatial frequency

$$\vartheta_c = \frac{d}{\lambda}\cos(\theta_c)\sin(\phi_c)$$

where d is the interelement spacing and λ is the wavelength. Note that for our MIMO system d is the spacing between elements of our virtual array. Also define the normalized Doppler frequency

$$\omega_c = f_c T_{PRI}$$

where T_{PRI} is the length of the (effective) PRI. The space-time steering vector of this clutter patch will be

$$\mathbf{v}_{nm} = e^{2\pi i\omega_c m} e^{2\pi i\vartheta_c n},$$

where m indexes the pulses and n indexes the array elements (and our indices start from 0).

Recall the relationship [14]

$$\omega_c = \left(\frac{2vT_{PRI}}{d}\right)\vartheta_c, \tag{19}$$

for a uniform linear array with no crab. We shift the data in the pulse domain by $\frac{-nd}{2vT_{PRI}}$ pulses. This will transform the steering vector to

$$\tilde{\mathbf{v}}_{nm} = e^{2\pi i\omega_c m}e^{2\pi in\left(\vartheta_c - \frac{\omega_c d}{2vT_{PRI}}\right)} = e^{2\pi i\omega_c m}$$

where the equality follows from (19). Thus in every Doppler bin, the clutter array response after doing this shifting is proportional to $[1,\ldots,1]^T$.

In general the required shift will be fractional. To implement it, we first apply a Taylor window that is translated the same amount we need to shift our signal, but in the opposite direction. After performing the shift, this window will be centered and will suppress some of the edge artifacts. The actual shift is implemented by taking an FFT, applying a phase ramp and applying an IFFT.

Ideally, after we perform this shifting, the clutter response in all of the virtual array elements would be identical. In practice, however, some mismatch still occurs due to hardware imprecisions, non-ideal aircraft motion, etc. We address the calibration and equalization of the system using a series of adaptive filters to match all of the virtual array channels to a reference channel. For a well-calibrated system, the filters would exhibit a thumbtack-like response with a magnitude of 1 in all channels, indicating the channels are well matched.

First, we create an adaptive FIR filter in the pulse domain. More precisely we choose a reference virtual array channel (empirically we found that transmit channel 3 in receiver 3 was the best), and use a Wiener-Hopf filter to match all the other channels to this reference channel. We use the data for all range bins to estimate the sample auto- and cross correlation (in the pulse domain). This is used to compute a filter that makes the data in each channel as similar as possible to the reference channel in a mean squared sense. This filter is applied in the pulse domain for each range bin. This filter can be viewed as a crude motion compensation that corrects for uncertainties in the velocity and exact phase center locations. The filter coefficient magnitudes are shown in Figure 14, where the plots in each row show the filter coefficient magnitudes for all the transmitters in a given receiver channel. Note that all the channels in receiver 1 (the first row), have been "turned down" by the filter. This receiver in general seems to be a persistent source of problems, which may be due to multipath resulting from its proximity to the aircraft wheels and wings (it was the foremost antenna, see Figure 8). Note that the absent plot in the $(3,3)$ position is the reference channel which is not filtered.

Next, we filter in the range domain to correct for phase errors in the transmitters and receivers. We first do a separate filter for each pulse, matching the range samples of each virtual array channel on each pulse to those of the reference channel. The filter coefficients are estimated separately for each pulse using only the samples from that pulse. The filter coefficients on one pulse are shown in 15(a). The single pulse range filters have broad peaks that are sometimes shifted from zero indicating that the receiver channels have slightly different delay paths and are correlated over multiple samples. The apparent correlation over multiple (roughly 2) samples is consistent with

the fact that the baseband signal which had a bandwidth of 10 MHz is sampled at 20 MHz. After applying this filter, we do another filter in range, here the same filter is applied to every pulse, but this is estimated using the samples from all pulses. The coefficients are shown in 15(b). These two filters seem redundant, but seem to perform slightly better than either alone.

The third filter is a two dimensional filter applied in range-Doppler space. Our interpretation of it is that it is basically matching the antenna patterns of all the virtual array elements. The two dimensional filter coefficients are plotted in Figure 16. Again, possibly as a result of multipath effects, receiver 1 requires significant adjustments to match the reference channel.

Lastly, we perform an FFT in fast time and apply a filter in the frequency domain. The filter coefficient magnitudes are show in Figure 17. This filter corrects for some sort of fast-time modulation which is occurring in some channels; in particular in receivers 1 and 2 (corresponding to rows 1 and 2), possibly due multipath off the wheels or wing.

The TDMA data is processed similarly. In the TDMA case, there are 720 pulses at the 6667 Hz PRF, but only one transmitter is transmitting on any given pulse. The virtual array extraction is accomplished by grouping the 720 pulses into 180 sets of 4 pulses. Then the receiver outputs for each set of 4 pulses are concatenated to yield the virtual array. The TDMA data is equalized in the same fashion as the DDMA data. The filter coefficient magnitudes for the pulse domain filter of the TDMA data is show in Figure 18. Note that in particular for transmitter 1 (the first column) the filter peaks are not quite as centered around 0 as they were for the DDMA data. This is because the filter is correcting for the fact that although we are treating the TDMA data as having been transmitted simultaneously, they were in fact transmitted on separated pulses.

5.2 SIMO EQUALIZATION

The same equalization strategy is employed to process the SIMO data, however, it is of course only applied to the receiver channels. Note that the adaptive equalization procedure has more freedom to correct errors after the fact for the MIMO system than the SIMO system since the MIMO system enables phase corrections across both the transmit and receive modules after the data collection. In contrast, for the SIMO system it is only possible to correct for phase differences or channel imbalance across the receive modules after the data has been collected. Thus the MIMO system allows more flexibility for calibration and is more robust to hardware errors. In general we noticed that the DDMA SIMO data was easier to calibrate than the conventional SIMO data. This can be seen in the pulse domain filter coefficients for the two types of SIMO data shown in Figure 19. Here each column is the CPI corresponding to a distinct scan angle, and each row is a different receiver. We are not certain why the conventional SIMO data is harder to calibrate. We speculate that it is due to the fact that the MIMO and the DDMA SIMO CPIs, having longer integration times, resolve the clutter with higher resolution than the conventional SIMO data. Since our calibration approach is calibrating to the clutter, it seems plausible that the the procedure would work better on data with longer integration times. Regardless, as we will show in the subsequent sections, the performance of the conventional SIMO data is quite poor in comparison to the DDMA SIMO data.

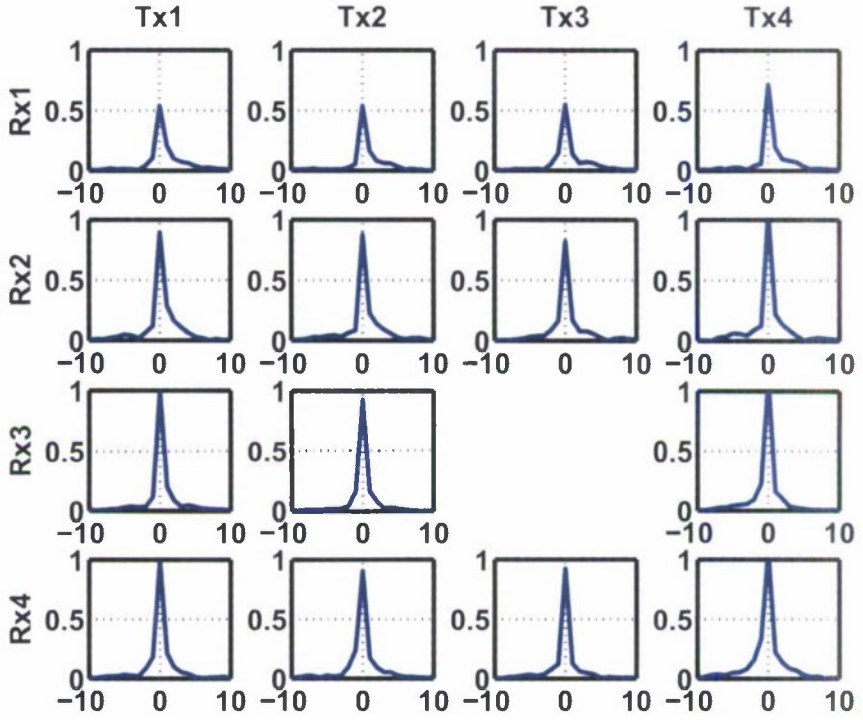

Figure 14. Pulse domain equalization filter coefficient magnitudes. Each row is a different receiver, each column is a different transmitter. The x-axis indicates pulses.

5.3 STAP

After equalization, the range-pulse-channel data cube is processed with PRI-staggered STAP [14]. Since we have shifted our data to align the clutter response across channels, in the STAP processing we must use steering vectors which have been transformed in the same fashion. The full space time steering vectors for a target with normalized Doppler ω_t and normalized spatial frequency ϑ_t is

$$\tilde{\mathbf{v}}_{nm}(\omega_t, \vartheta_t) = e^{2\pi i \omega_t m} e^{2\pi i n \left(\vartheta_t - \frac{\omega_t d}{2vT_{PRI}}\right)}.$$

Let N_p be the number of pulses. For each channel we take K contiguous subsets of length $N_p - K$ and Doppler filter them. Thus for each Doppler bin we have a vector of length NK, where N is the number of array elements (virtual array elements in the MIMO case). These staggered Doppler filters are applied to the full space time steering vectors to obtain steering vectors for the PRI-staggered STAP processing. We also apply the same staggered Doppler filters to the data. So for each range-Doppler bin of the data we have a vector of length NK.

The STAP filters require an estimate of the clutter covariance matrix. The process of estimating this matrix is called training. Let us now describe our training strategy. For a fixed Doppler bin,

let $\mathbf{A}$ denote $n_{range} \times N$ matrix (where n_{range} is the number of range samples we have processed), whose columns have the data from the array channels in that Doppler bin for all the ranges. Here for selecting training data we use a single Doppler filter, hence there are only N and not NK degrees of freedom. We perform a singular value decomposition and write

$$\mathbf{A} = \mathbf{USV}^H.$$

The eigenvectors of the sample virtual array covariance are the columns of $\mathbf{V}$. The eigenvector corresponding to the largest eigenvalue should be the clutter response which should be approximately $[1, \ldots, 1]^T$. Let

$$\mathbf{W} = \mathbf{US}.$$

The components of each row of $\mathbf{W}$ express the contribution of each eigenvector (column of $\mathbf{V}$) to the expansion of that range-Doppler cell in the basis of eigenvectors. Let $\mathbf{T}$ be the length n_{range} vector with

$$\mathbf{T}_n = \frac{\sum_{m=2}^{N} |\mathbf{W}_{nm}|^2}{\sum_{m=1}^{N} |\mathbf{W}_{nm}|^2}.$$

The n^{th} component of $\mathbf{T}$ is the ratio of the contribution to the data in the n^{th} range-Doppler cell of the subdominant eigenvectors alone versus the clutter and subdominant eigenvectors. We take range bins with smaller values of $\mathbf{T}_n$ to use as training samples with the expectation that these have strong sources of clutter. This is essentially a type of phase selective training [15].

We use the selected range bins to compute a sample covariance matrix of the PRI staggered Doppler filtered data for that Doppler bin (note this covariance matrix will be $n_R n_T K \times n_R n_T K$ where K is the number of stagger). When we compute the STAP weights, we iterate through the range bins that we are processing and if the range bin under consideration or any range bins slightly above or below that range bin were used as a sample for the covariance matrix, we perform a low rank update to remove its contribution to the covariance matrix[4]. We compute the 75^{th} percentile of the distribution of power across all range bins at that Doppler. For range bins whose power is greater than this level, we do not fully remove the contribution to the sample covariance matrix, but leave a contribution to the the sample covariance matrix proportional to the power of the cell. This helps desensitize the STAP processor to clutter discretes. This technique is known as power selective de-emphasis [16]. For the MIMO data we use $K = 4$ staggers, for the SIMO data we use $K = 16$, this give the MIMO and SIMO the same number of adaptive degrees of freedom (though the MIMO has more spatial degrees of freedom).

We apply noise loading for further robustness. To estimate the noise covariance, we sample noise only data using range bins early in the PRI before any signal has been returned by the ground. The same filters used to equalize the data are applied to the noise and the filtered noise covariance is used to load the clutter covariance when we compute the STAP weights.

---

[4] We do this using the Sherman-Morrison-Woodbury formula,

$$(\mathbf{R} + \mathbf{YXZ})^{-1} = \mathbf{R}^{-1} - \mathbf{R}^{-1}\mathbf{Y}(\mathbf{X}^{-1} + \mathbf{Z}^H\mathbf{R}^{-1}\mathbf{Y})^{-1}\mathbf{Z}^H\mathbf{R}^{-1}.$$

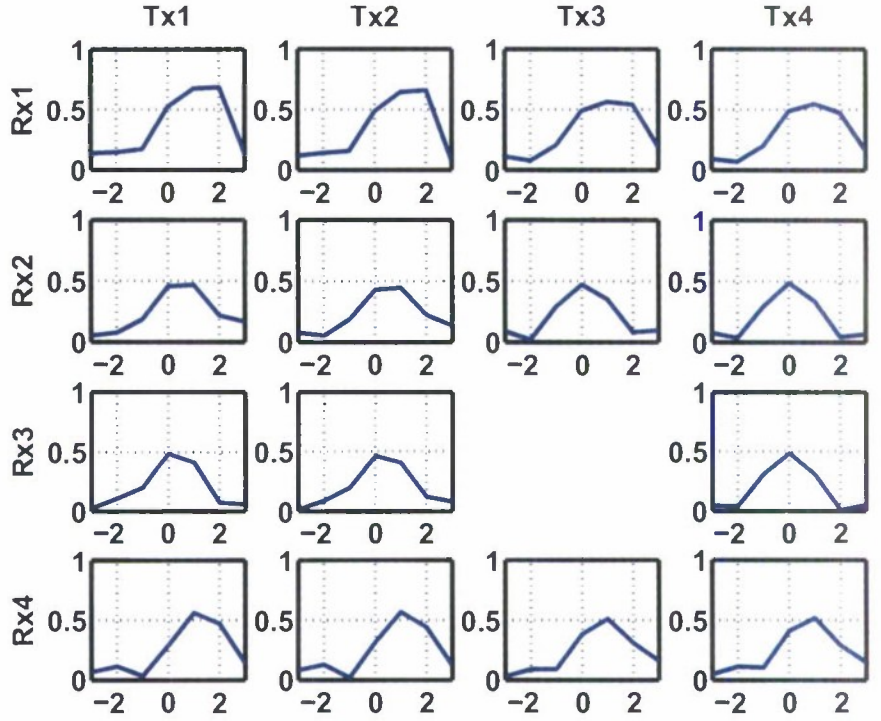

(a) Range domain filter coefficient magnitudes for a single pulse.

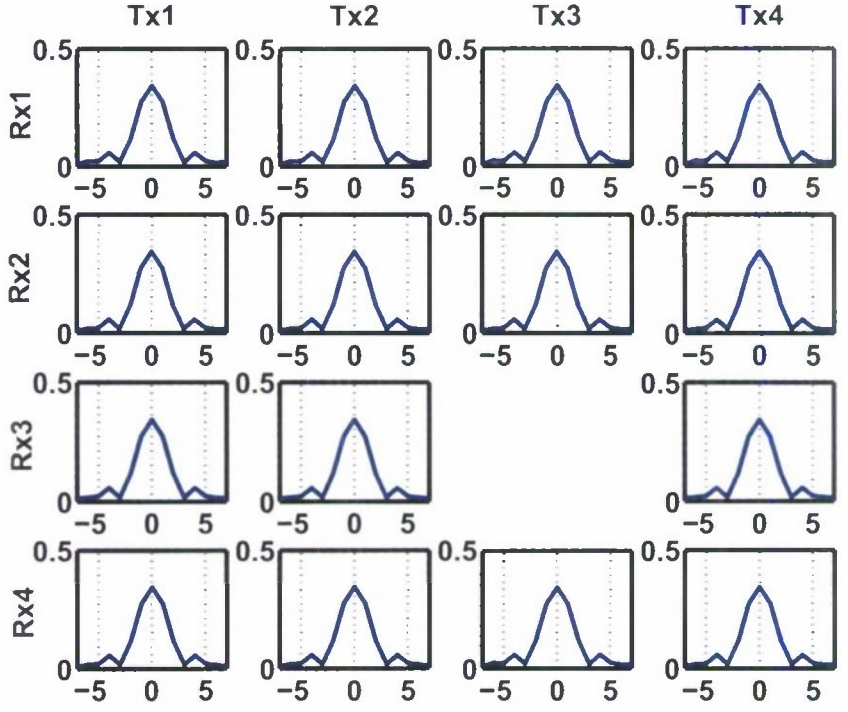

(b) Second range domain filter coefficient magnitudes using all pulses.

Figure 15. Range domain equalization filter coefficient magnitudes. The x-axis is fast time samples.

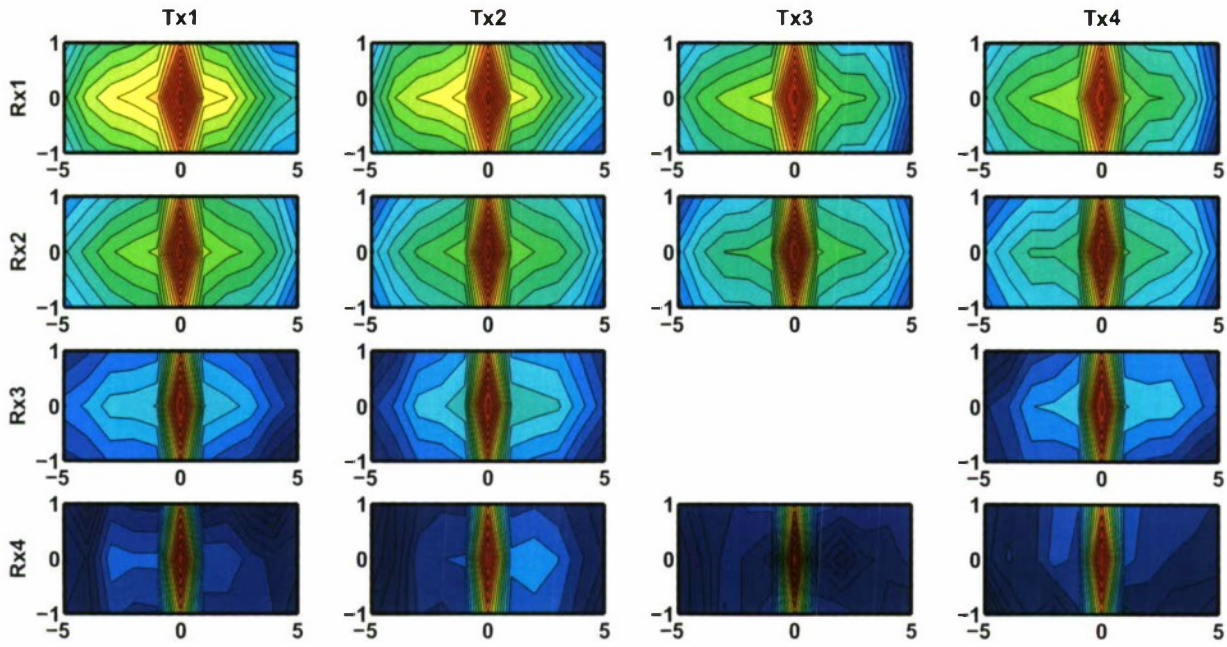

Figure 16. Two dimensional filter coefficient magnitudes. The x axis is Doppler bins and the y axis is range.

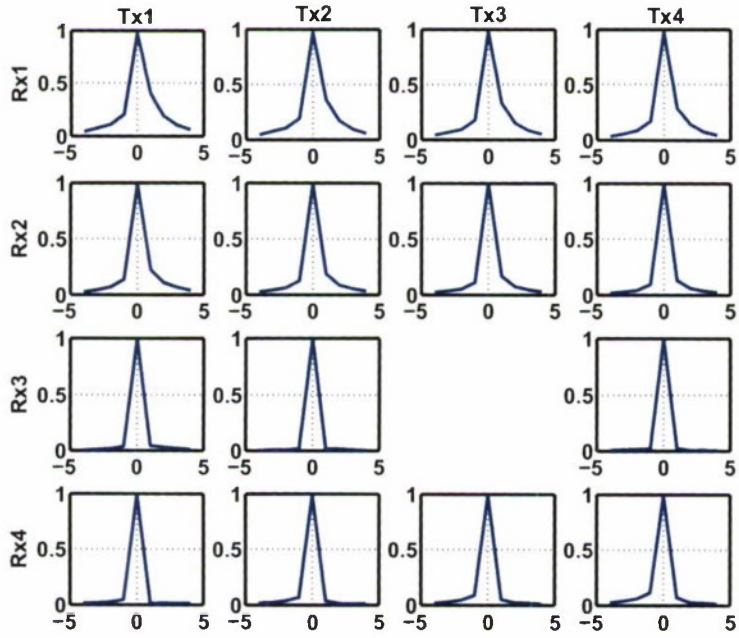

Figure 17. Fast-time frequency domain filter coefficient magnitudes.

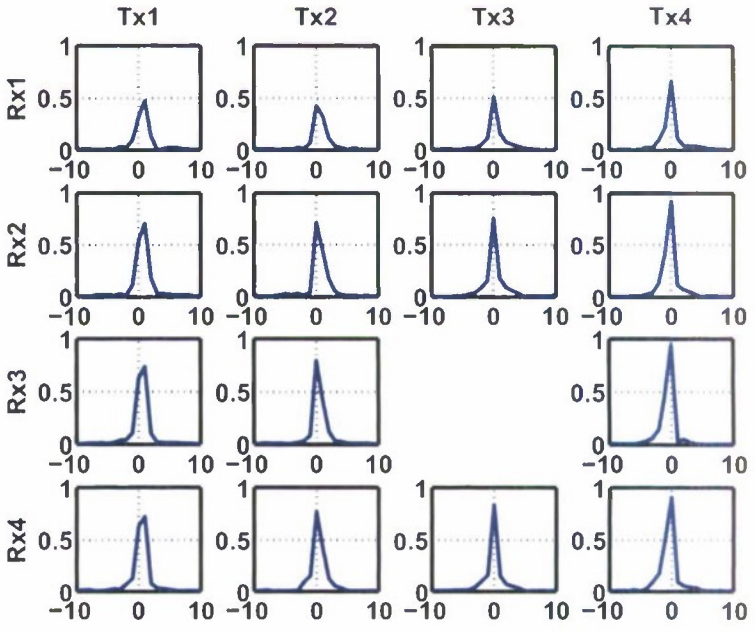

Figure 18. TDMA pulse domain filter coefficient magnitudes.

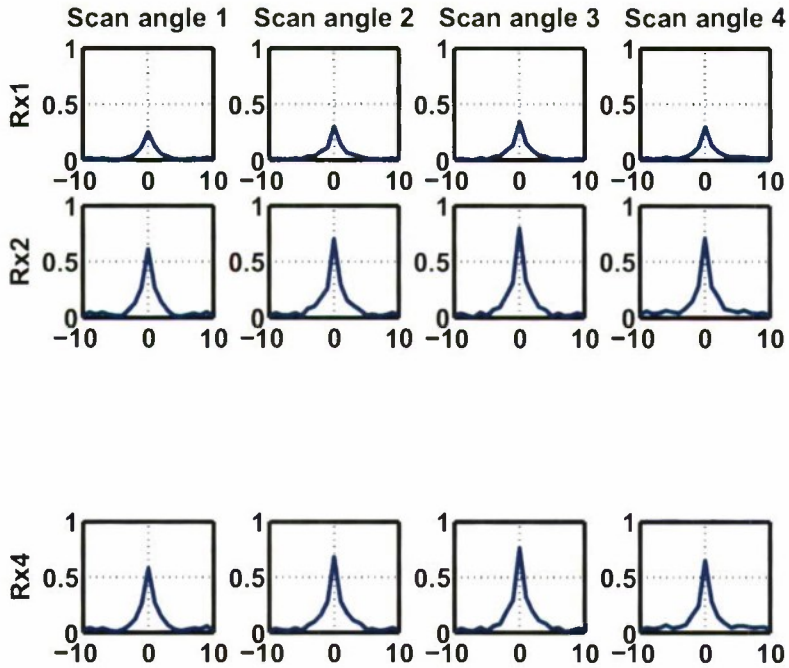

(a) Pulse domain filter coefficient magnitudes for DDMA SIMO data.

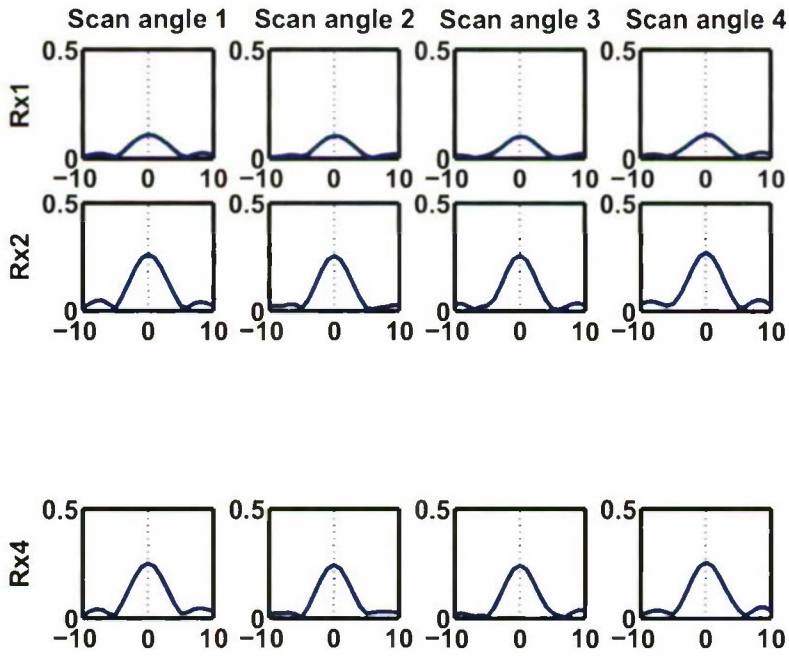

(b) Pulse domain filter coefficient magnitudes for conventional SIMO data.

Figure 19. Pulse domain filter coefficient magnitudes for two types of SIMO data.

6. EXPERIMENTAL RESULTS

Figures 20, 21, and 22 show a region of a range-Doppler map for a single dwell of DDMA SIMO data (dense receive array), DDMA MIMO data (sparse receive array), and conventional SIMO data (dense receive array) respectively, after PRI-staggered STAP. In the DDMA SIMO case, a dwell consists of the four interleaved CPIs covering four distinct scan angles, while for the MIMO system a dwell is a single CPI covering the same total scan area. For the conventional SIMO data, a dwell is a sequence of non-interleaved consecutive CPIs covering four distinct scan angles. In order to concisely display detections across the entire test area, in Figures 20, 21, and 22 we show the maximum over the AMF normalized STAP outputs for a collection of receive beams covering the test site. In the plots of the SIMO data, to combine the multiple scan angles, we take the maximum over the post-STAP data from all four scan angles as well as over the collection of receive beams. The labels $V1, \ldots, V4$ indicate the GPS-derived locations of the instrumented vehicles from the experiment and the white rectangles indicate detections after a local CFAR normalization is applied (not pictured) with a detection threshold level of 10 dB.

The number of PRI staggers for the STAP algorithm, $K = 16$ staggers for SIMO and $K = 4$ staggers for MIMO, were chosen to achieve the same number of adaptive degrees of freedom for both processing approaches. In this example, the MIMO system clearly detects three of the four vehicles in the experiment while the DDMA SIMO system only detects one of the four vehicles. The conventional SIMO system does not satisfy the detection criteria for any vehicles, although vehicle 1 can be seen to be visible somewhat above the clutter.

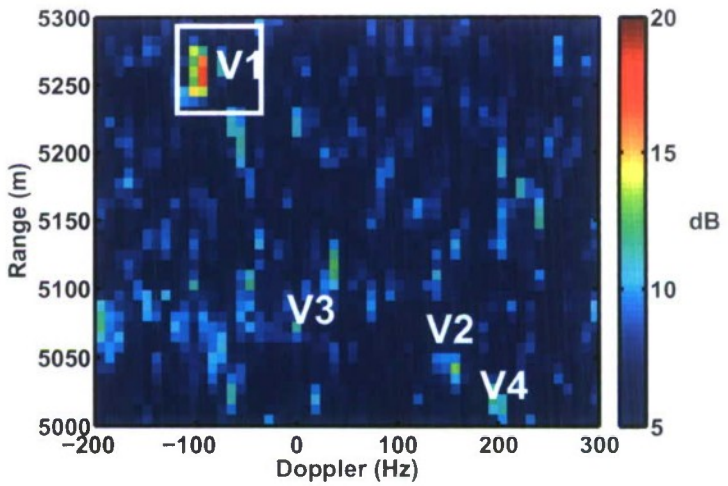

Figure 20. DDMA SIMO detection results for four instrumented vehicles after adaptive processing of a single dwell.

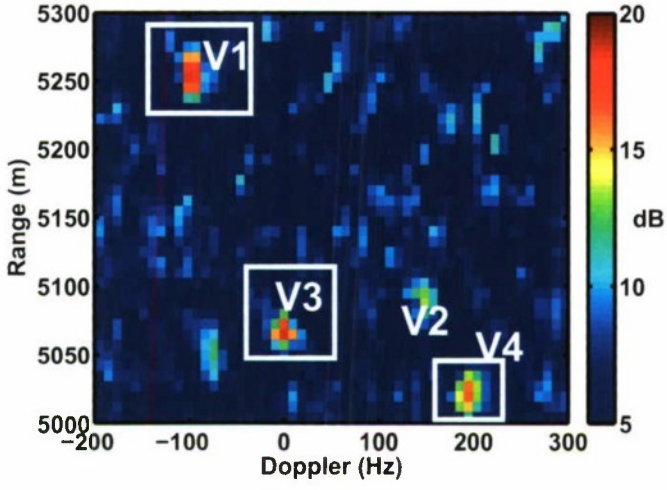

Figure 21. DDMA MIMO detections for four instrumented vehicles after adaptive processing in a single dwell.

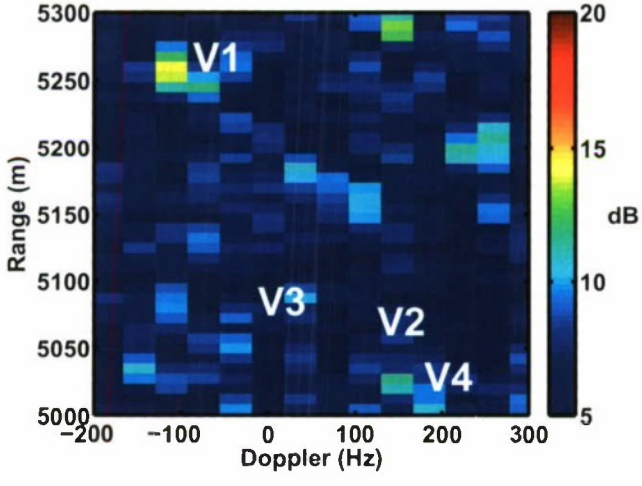

Figure 22. Conventional SIMO post STAP. No targets satisfy the detection criteria.

Because the plots in Figures 20, 21, and 22 combine multiple receive beams (which are not all pointed broadside), the target Dopplers do not show how close to the clutter the targets are. In Figures 23 and 24, we display the MVDR normalized output for one receive beam pointed at V1 and V3. We have set the clutter at that angle to correspond to 0 m/s. In these plots, it can clearly be seen that the high velocity of V1 ensures it is far from the clutter notch and thus detectable by both systems, while the wider clutter ridge for the SIMO configuration obscures the slower V3.

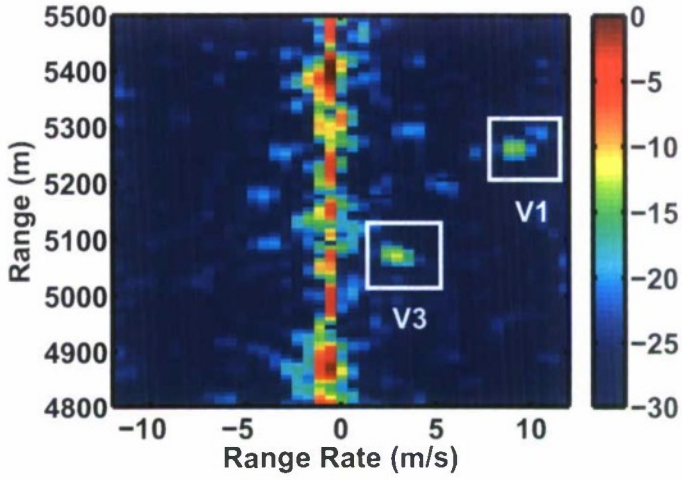

Figure 23. DDMA MIMO MVDR beamformer output at one angle.

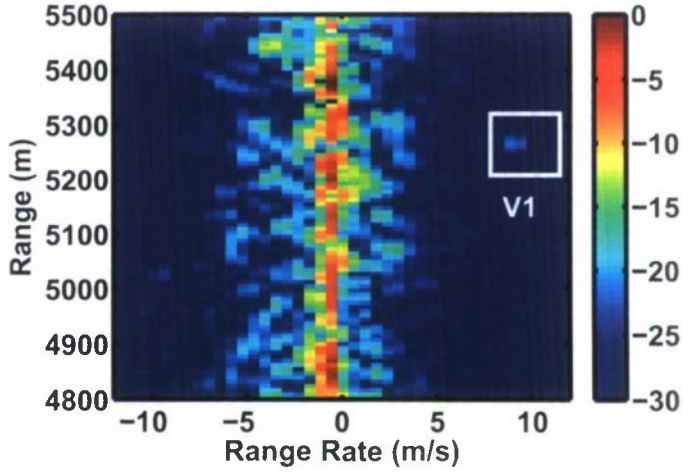

Figure 24. DDMA SIMO MVDR beamformer output at one angle.

The test site was surrounded by trees, so some of the vehicles may be shadowed at times. However, recall that for this DDMA MIMO vs DDMA SIMO comparison, the data was co-collected (in fact, the same dwell of data is used for both DDMA SIMO and DDMA MIMO – they differ only in the receive channels and data processing techniques used), so that any shadowing in the dwell affects the DDMA SIMO and DDMA MIMO cases equally. The conventional SIMO data was interleaved and the dwell depicted in Figure 22 occurs 0.1 seconds after the dwells processed for the DDMA MIMO and DDMA SIMO cases. Therefore, this example demonstrates a substantial

improvement in detectability for vehicles $V3$ and $V4$ using the MIMO techniques. In Figure 25(b) we plot the SINR of the slowest vehicle, $V3$, as a function of time for the DDMA MIMO and DDMA SIMO systems. This illustrates the uniform improvement in SINR for slow moving targets using the MIMO approach. In Figure 25(a) we plot the velocities of all the vehicles over the course of the run. Figures 20, 21, 22, 23, and 24 correspond to $t \sim 0.2$ seconds. Note that $V1$ was traveling much faster than the other vehicles explaining why it was detected by the SIMO systems.

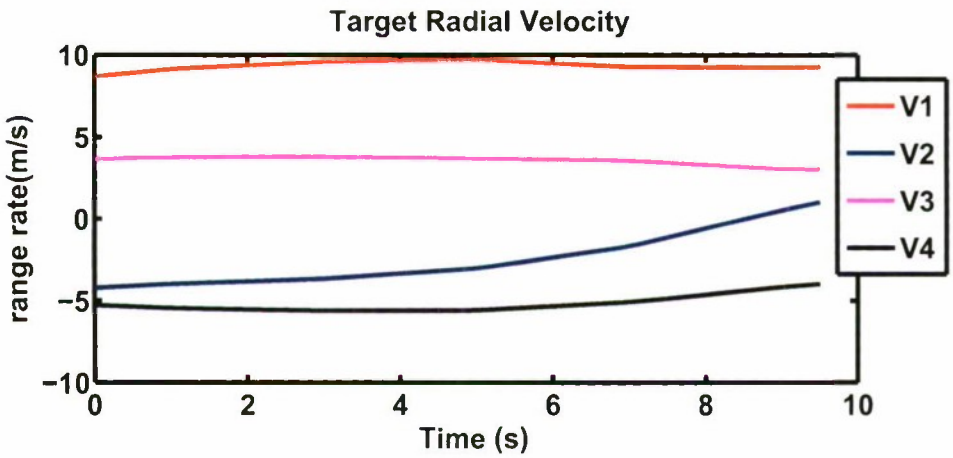

(a) Target radial velocities over time (does not include platform motion).

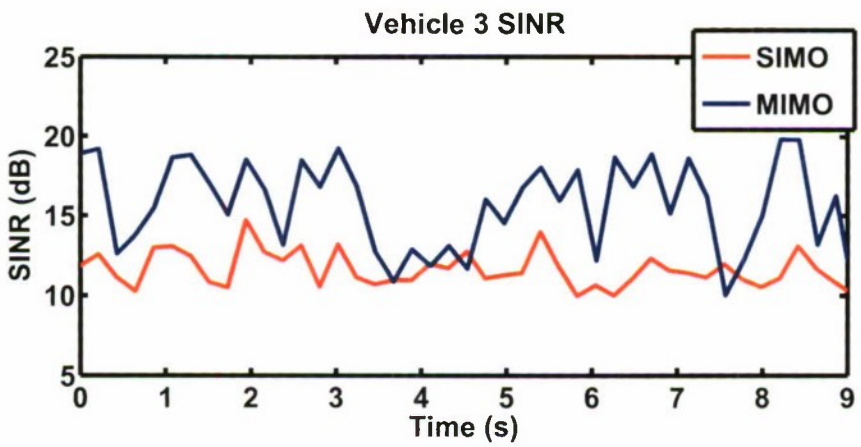

(b) Vehicle 3 SINR over time.

Figure 25. Target SINR (for vehicle 3) and radial velocity (all targets) over time.

Some of the recorded data involved four dismount targets. Two of the dismounts were carrying a large corner reflector. Although the unaugmented dismounts were not visible, the dismounts carrying the corner reflector (D2 and D3) provide a target with a comparable RCS to the vehicles, but moving much slower. In Figures 26(a) and 26(b) we plot post-STAP MVDR beamformer outputs

of the area around the dismounts. The MIMO system can distinguish the moving corner reflector from the clutter while the DDMA SIMO system cannot. In Figures 27(a) and 27(b) we plot the GPS derived velocity of the dismounts carrying the reflector, and the output SINR vs time.

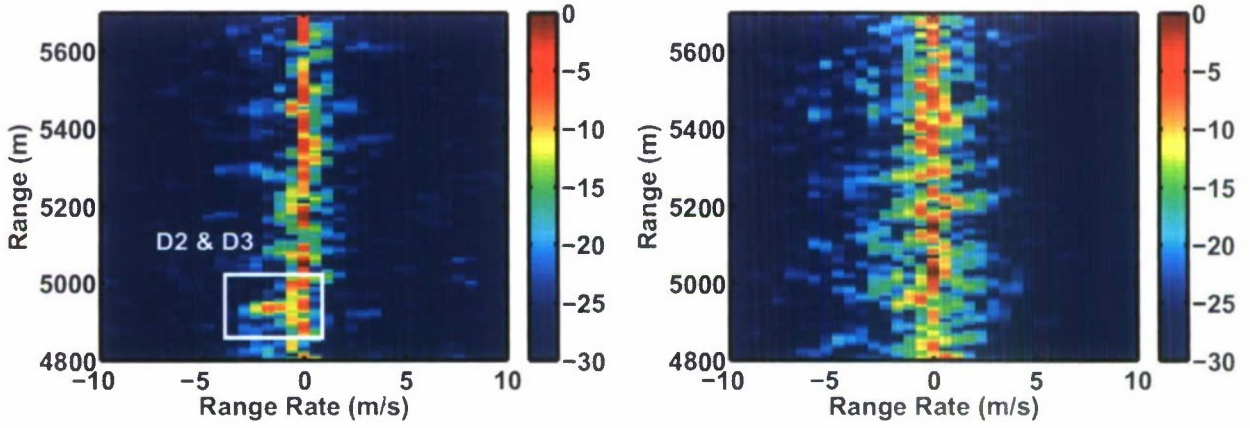

(a) MIMO dismount detections.

(b) SIMO dismount detections.

Figure 26. MVDR beamformer output showing dismounts D2 and D3 who were carrying a large corner reflector between them are clearly visible to the MIMO system but not the SIMO system.

6.1 MEASURED SINR LOSS

The expected MDV of the two architectures can be compared by looking at the signal-to-interference-plus-noise ratio (SINR) loss versus radial velocity. First recall that

$$SINR = \frac{|\mathbf{w}^H \mathbf{x}|^2}{\mathbf{w}^H \mathbf{R}_{i+n} \mathbf{w}},$$

where $\mathbf{w}$ are the adaptive weights, $\mathbf{x}$ is a synthetic target, and $\mathbf{R}_{i+n}$ is the interference-plus-noise covariance matrix. The SINR loss is the ratio of the observed SINR to the SNR in the noise-only case. To calculate the SINR loss from the measured data, the adapted weights $\mathbf{w}$ and covariance $\mathbf{R}_{i+n}$ are estimated from a single CPI of data over a set of radial velocities. To estimate the noise-only covariance matrix, we use noise-only range bins recorded before any ground returns are received and apply the previously computed adaptive equalization filters.

In [8] theoretical bounds on achievable SINR loss for MIMO and SIMO systems were derived. The model used to compute these bounds assumes rank 1 clutter in each Doppler bin, infinite CNR, exact knowledge of the covariance matrix, and no internal clutter motion or mutual coupling. The bounds are only valid in a neighborhood of the clutter notch.

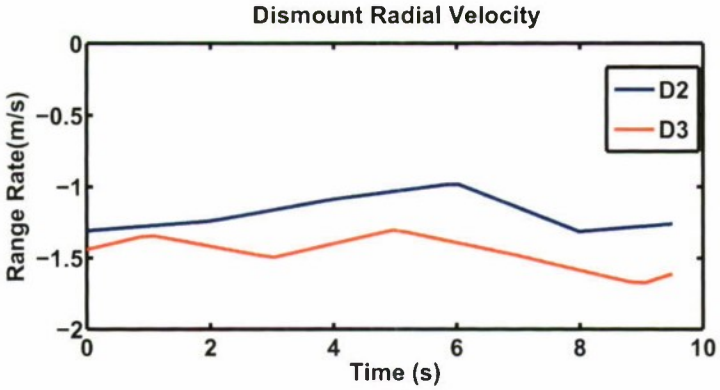

(a) Radial Velocity of dismounts carrying the corner reflector (does not include platform motion).

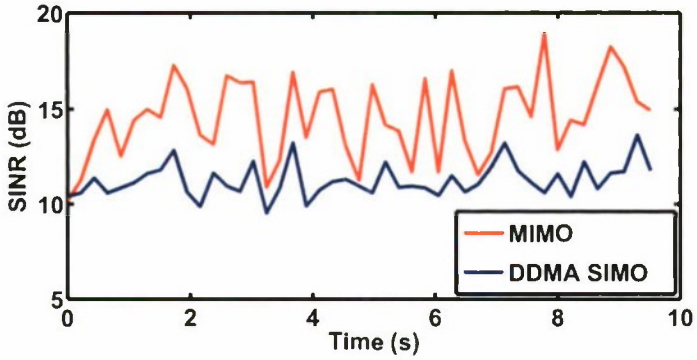

(b) Moving corner reflector SINR as a function of time.

Figure 27. Target SINR for corner reflector and radial velocity for dismounts carrying reflector.

In Figure 28, the solid lines show the estimated SINR loss for the experimental MIMO and SIMO systems at an azimuthal angle of 0 degrees as a function of target radial velocity. The dashed lines indicate the theoretical bound on SINR loss for the MIMO and SIMO systems as derived in [8]. Observe that the MIMO system clearly has a much narrower notch and avoids the blind velocities that would be typical of a sparse aperture with conventional processing. This performance demonstrates the advantage of the large filled virtual aperture. Also observe that while the experimental curves do not quite meet the bounds, the overall improvement of our MIMO system over our SIMO system is in line with the improvement that one would expect based on the theoretical curves. Note that although the TDMA waveforms have very good performance, the DDMA waveforms appear to perform slightly better. However, we should point out the TDMA data was not interleaved and was collected on a different run which could be the source of the performance difference (for example, possibly due to more severe crab). Also note that the conventional SIMO data has poorer performance than the DDMA SIMO data. The difference in the performance of the two types of SIMO data is likely due to calibration difficulties noted in Section 5.2. We present some addition discussion of these performance differences in Section 7.

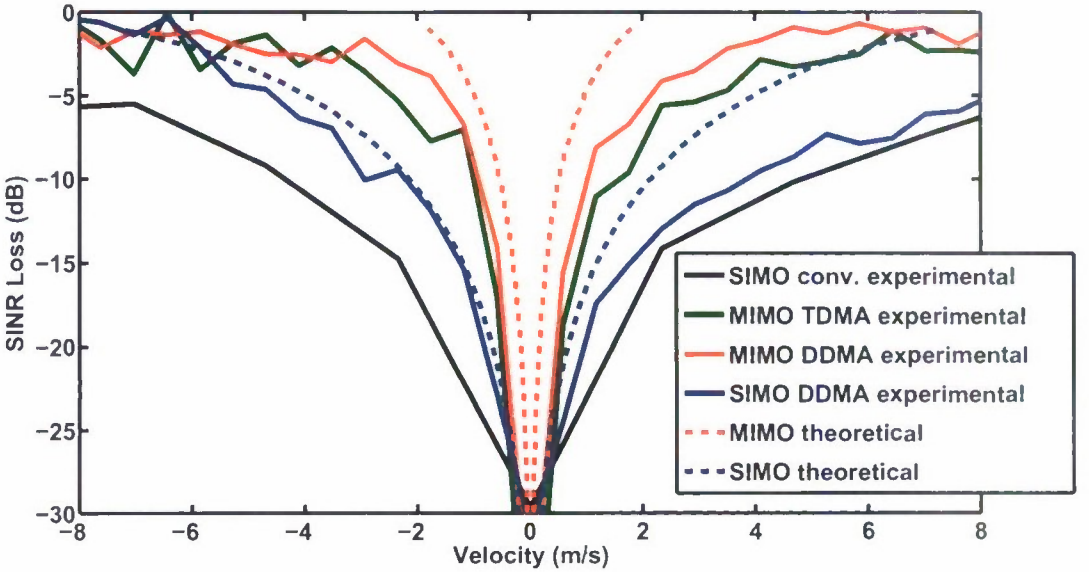

Figure 28. SIMO and MIMO experimental and theoretical SINR Loss curves at azimuthal angle 0. Here the SIMO curve is the conventional (non DDMA) SIMO data.

6.2 RECEIVER OPERATING CHARACTERISTIC CURVES

In Figure 31, we show ROC curves for the DDMA MIMO and DDMA SIMO data. This was computed using data from a run consisting of 45 sequential CPIs over the course of 10 seconds. Note that although the absolute performance is low, the MIMO systems exhibits an order of magnitude improvement in performance at $P_D = 0.5$. The curve does not take into acount shadowing by trees surrounding the site which we expect meant that at on average only two or at most three vehicles would be unobscured at any given time. To illustrate this, Figure 29 depicts the paths of the vehicles during the experiment. Figure 30 is a frame of video showing a vehicle, that is in the same position as vehicle 4 in Figure 29, driving near the tree line. The two sources of shadowing that were most problematic were the trees at the bottom of the circular path, and the trees lining the road that vehicle 1 was driving along. Given this shadowing, the MIMO performance for our low cost testbed is quite good.

6.3 ANGLE ESTIMATION ACCURACY

In this section, we consider the angle estimation performance of the large sparse MIMO array in comparison to the smaller SIMO array. Let $\mathbf{v}(\theta)$ and $\mathbf{w}(\theta)$ denote the adapted weight and steering vectors as a function of angle in a given Doppler bin (recall we are using a PRI-staggered STAP

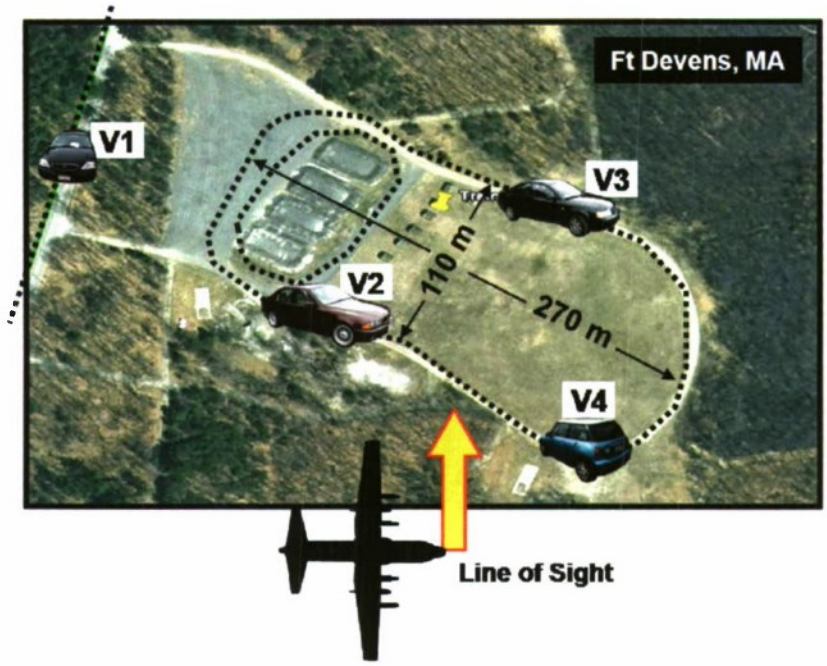

Figure 29. Test site and vehicle paths.

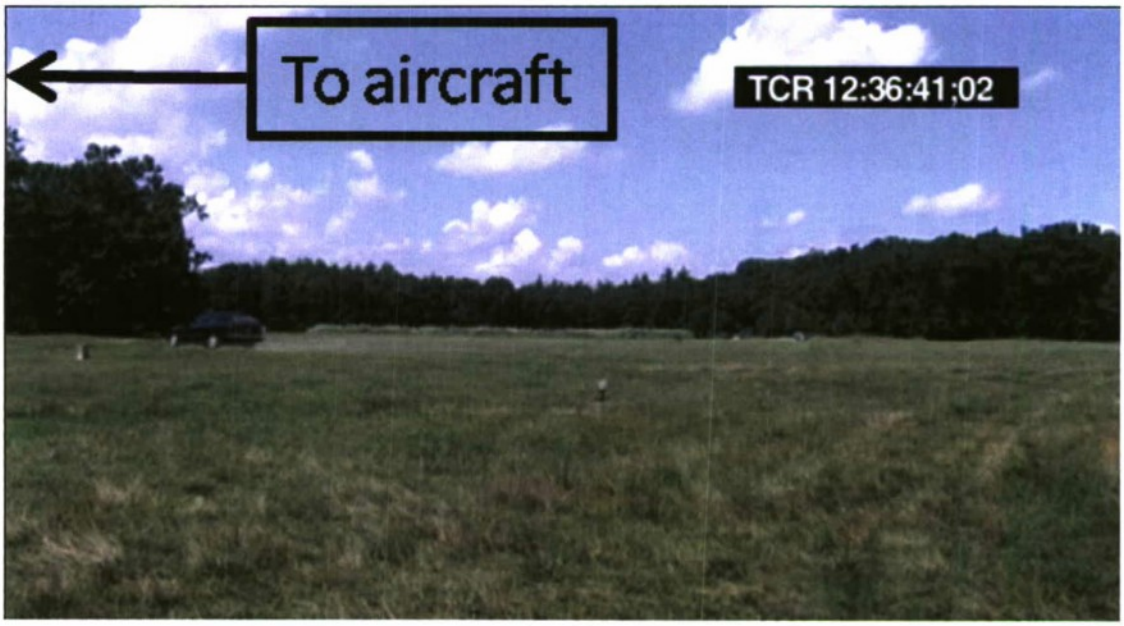

Figure 30. Vehicle driving near tree line.

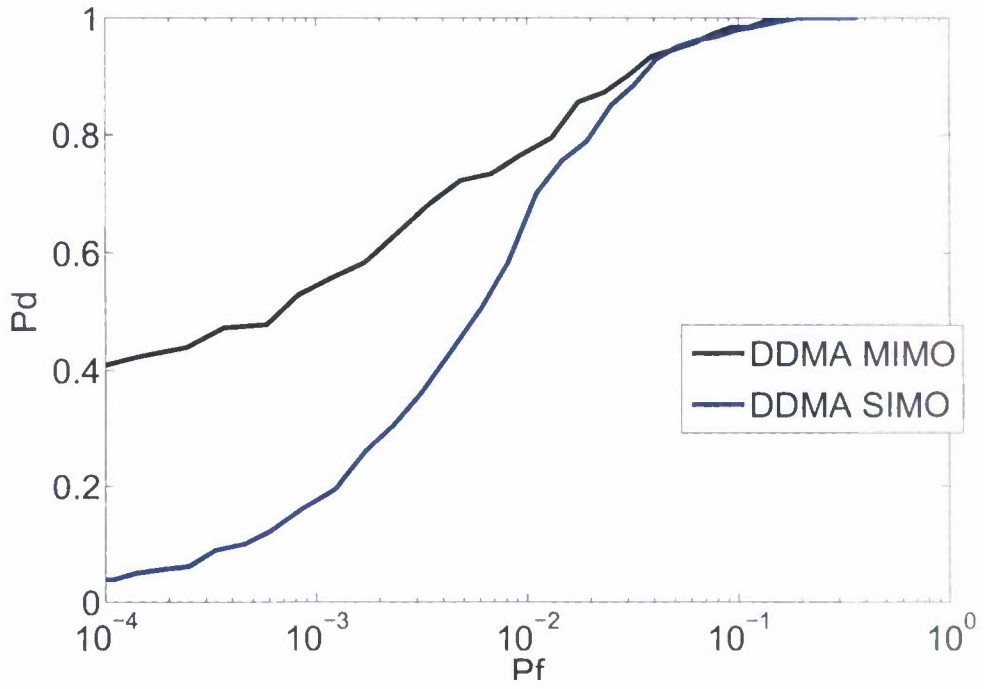

Figure 31. ROC curves for DDMA SIMO and DDMA MIMO data.

algorithm). Assume that $\mathbf{w}(\theta)$ is AMF normalized, i.e.,

$$\mathbf{w}(\theta) = \frac{\mathbf{R}^{-1}\mathbf{v}(\theta)}{\sqrt{\mathbf{v}(\theta)^H \mathbf{R}^{-1}\mathbf{v}(\theta)}}.$$

Suppose our data vector $\mathbf{x}_0$, is distributed as

$$\mathbf{x}_0 = \alpha\mathbf{v}(\theta_0) + \mathbf{n}$$

with $\mathbf{n}$ a multivariate complex Gaussian with covariance

$$E[\mathbf{n}\mathbf{n}^H] = \mathbf{R}.$$

Then the estimator

$$\hat{\theta} = \arg\max_{\theta} |\mathbf{w}(\theta)^H \mathbf{x}_0|^2 = \arg\max_{\theta} \frac{|\mathbf{v}(\theta)^H \mathbf{R}^{-1}\mathbf{x}_0|^2}{\mathbf{v}(\theta)^H \mathbf{R}^{-1}\mathbf{v}(\theta)} \tag{20}$$

is the maximum likelihood estimate of the target direction θ_0. Consider the function

$$\Psi(\theta) = |\mathbf{w}(\theta)^H \mathbf{v}(\theta_0)|^2.$$

We call this the array ambiguity function. It is what the function being maximized in (20) tends to at high SINR[5].

[5] Note that this is not the adapted beam pattern, which is

$$b(\theta) = \mathbf{w}(\theta_0)^H \mathbf{v}(\theta),$$

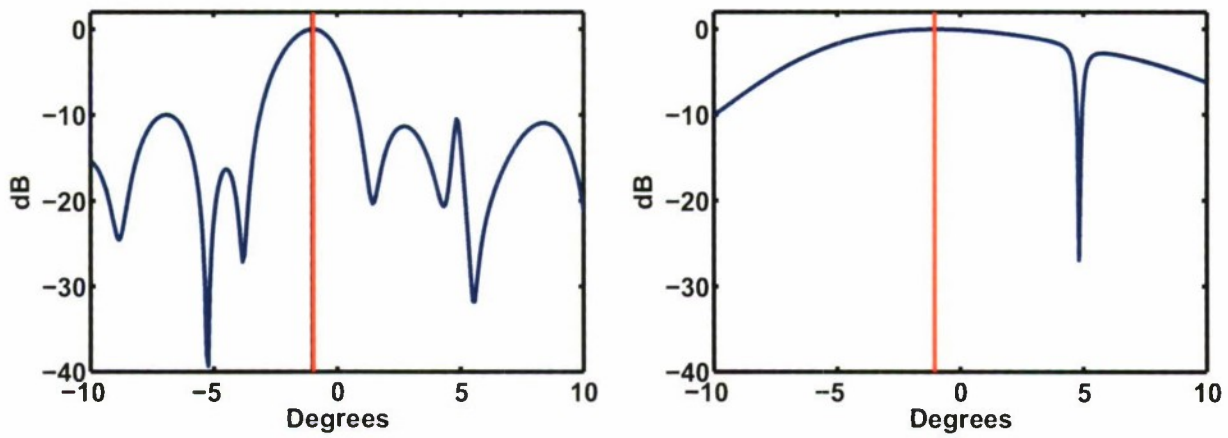

(a) MIMO array ambiguity function.

(b) SIMO array ambiguity function.

Figure 32. Slice of SIMO and MIMO array ambiguity function steered to -1 degrees.

In Figure 32, we plot the array ambiguity function in a single Doppler bin (corresponding to the response to a target at -1 degrees with a velocity of 7 m/s). We use the same covariance estimate that was used in the STAP processing. Note that the MIMO system has a much narrower peak as expected, which will yield improved angle estimation performance. For comparison, the (nonadaptive) MIMO virtual array should have a peak-to-null beamwidth of 2.38 degrees while the nonadaptive SIMO array should have a peak-to-null beamwidth of 9.58 degrees. Also for comparison, in Figure 33 we plot the array ambiguity function in the case there is no adaptation (i.e., when $\mathbf{R} = \mathbf{I}$).

Although the ground vehicles were instrumented, direct assessment of the angle estimation performance is difficult due to several factors. First, our radar data samples in the testbed are not synchronized to the plane's navigation data, so we had to estimate the time alignment. We did this by first generating a crude SAR image from the radar data and then mapping a USGS map of the test site into range-Doppler space, based on an initial guess of the time offset. We varied this guess until the two images matched. This process was done by eye and so we are unlikely to have much better than about 1 second alignment between the GPS and radar data. While this coarse alignment was fine for matching detections with the instrumented targets, it is not sufficient for measuring the angle estimation performance. Furthermore, the IMU unit in the aircraft was aligned with the array axis by hand, so a few degrees misalignment is likely. This leaves us some doubts about the accuracy of the measured crab. These uncertainties make comparison of the angle estimates for detected targets with the navigation data difficult.

i.e., in the beam pattern we compute a fixed weight and vary the input signal. For the array ambiguity function we fix the signal and vary the weight.

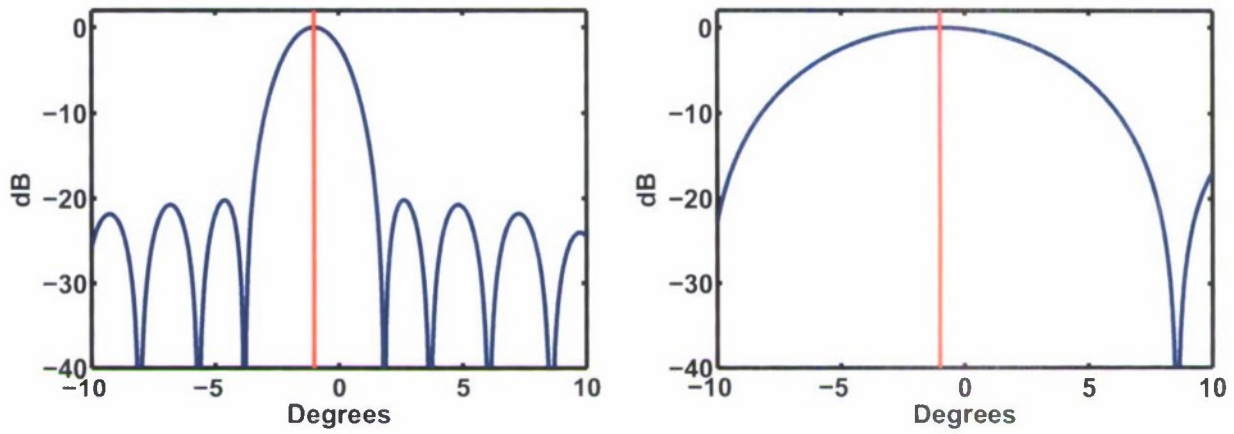

(a) MIMO unadapted array ambiguity function.

(b) SIMO unadapted array ambiguity function.

Figure 33. Slice of SIMO and MIMO unadapted array ambiguity function steered to -1 degrees.

Despite of these uncertainties, in Figure 34(a) we plot some rough estimates of the angle estimation error for one vehicle (V1) over a two second period and in 34(b) we plot the SINR of this vehicle. In Figure 35, we do the same for the SIMO case. This target and time period were chosen because both the MIMO and SIMO processing techniques detected the vehicle during this period. The MIMO system clearly gives much more consistent estimates.

An interesting and obvious feature of both the MIMO and SIMO case is they seem to be biased somewhat negatively, the SIMO more-so than the MIMO. There are at least four sources possibly contributing to this bias. First, the measured crab over the course of the run is between 1.8 and 2.1 degrees. This has not been taken into account in our angle estimation, however, we also are not certain that this measured crab is correct. Secondly, inaccuracy in how our radar data is time aligned with the navigation data will contribute a source of error to the angle estimation. In Figure 36, we plot the MIMO array response (in a single Doppler bin) to a synthetic target at -1 degrees (indicated by the black line) but now with a velocity of around 1.2 m/s which is much closer to the clutter than the synthetic targets in Figures 32(a) and 32(b). The actual peak of this slice is indicated by the red line which is 0.63 degrees to the left of where the beam is steered. This can be a source of bias. The same thing happens in the SIMO case when the target is near the clutter. Similarly, calibration errors which we know are present will introduce steering vector mismatch which will produce additional sources of errors.

These sources of error are certainly all present to some degree and unfortunately due to the limitations of our testbed and experimental setup, we cannot estimate them well enough to give a precise measure of the performance improvement of the MIMO system. The plots shown, however, qualitatively indicate the MIMO system's improved angle estimation capability.

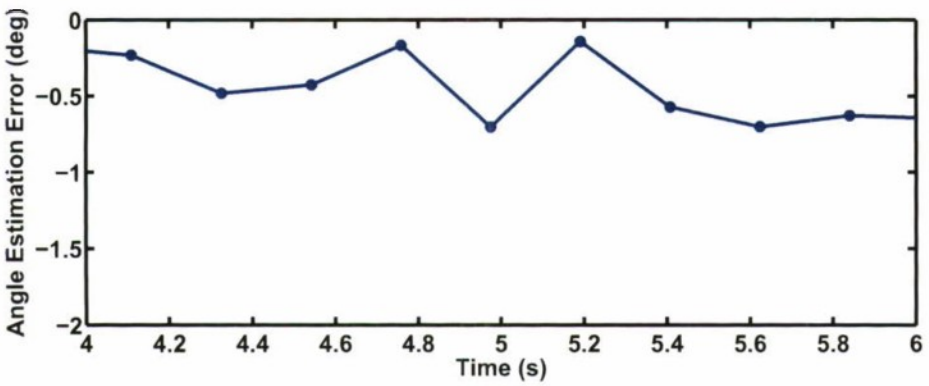

(a) MIMO angle estimation error for vehicle 1.

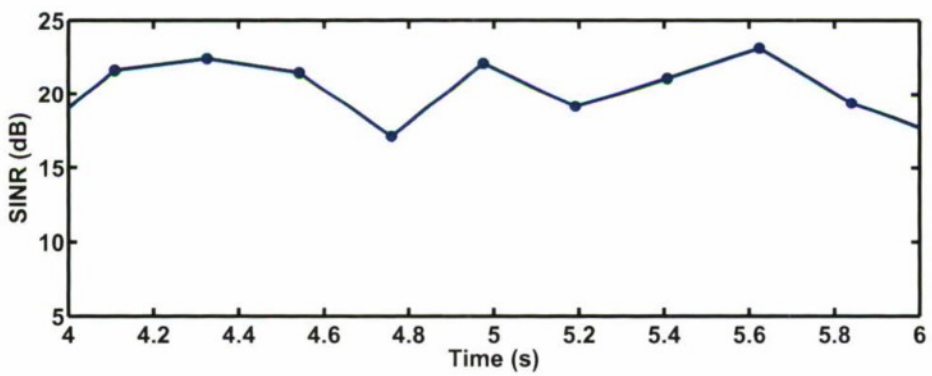

(b) MIMO SINR for vehicle 1.

Figure 34. MIMO angle estimation error and SINR for vehicle 1 during two second period.

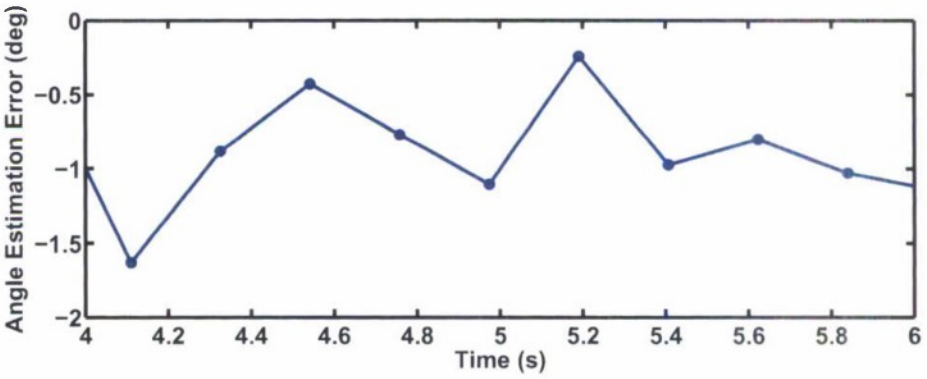

(a) SIMO angle estimation error for vehicle 1.

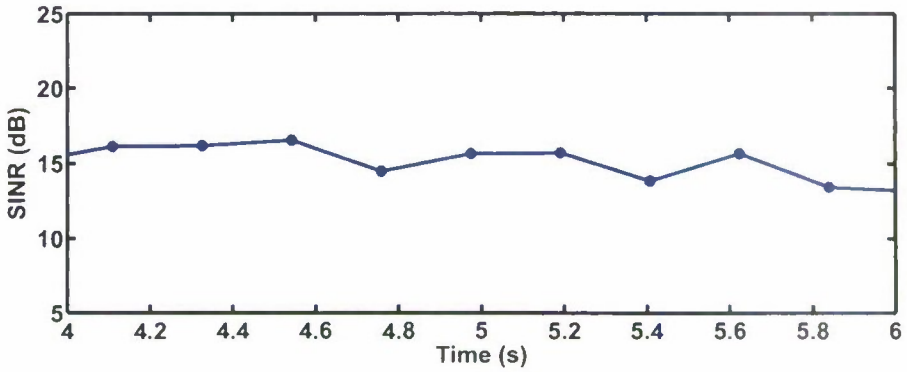

(b) SIMO SINR for vehicle 1.

Figure 35. SIMO angle estimation error and SINR during two second period.

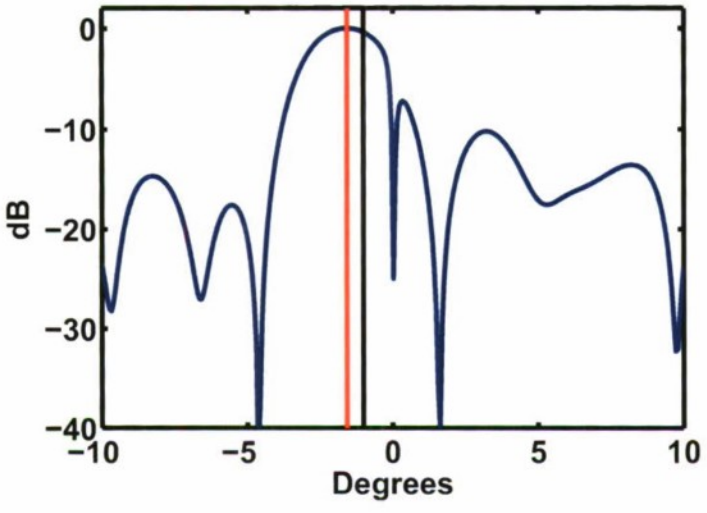

Figure 36. Slice of MIMO array ambiguity function steered to -1 degrees (black line). Actual peak is the red line.

7. MIMO AND SIMO COMPARISON ISSUES

There are many differing opinions of what a fair "apples" to "apples" comparison is for a MIMO versus SIMO GMTI radar system. In this section, we make some observations about the differences in experimental performance of the MIMO and SIMO systems. We also make some general observations about the evaluation of the applicability of MIMO techniques to a given task.

In Section 6.1, we compared our experimental SINR loss to some theoretical optimum SINR loss curves of [8]. It will be useful in our subsequent discussion to examine the expressions for these curves more explicitly. Assume that our transmit and receive arrays are linear and our coordinates are chosen so they lie on the x-axis in $\mathbb{R}^3$. Let x_i^R $(i = 1, \ldots, n_R)$ and x_j^T $(j = 1, \ldots, n_T)$ be the x-coordinates of the transmitter and receiver phase center locations and assume

$$\sum_{i=1}^{n_R} \sum_{j=1}^{n_T} x_i^R + x_j^T = 0,$$

where n_R, n_T are the number of receivers, transmitters. This simply means we choose our coordinates so that the virtual array is centered about 0. Define

$$\mathcal{A} = n_T^{-1} n_R^{-1} \frac{16}{\lambda^2} \sum_{i=1}^{n_R} \sum_{j=1}^{n_T} \left(x_i^R + x_j^T \right)^2 .$$

Let $\mathcal{T}$ be the set of times at which each pulse is transmitted. Assume

$$\sum_{t \in \mathcal{T}} t = 0$$

and define

$$\rho = \frac{64}{n_D \lambda^2} \sum_{t \in \mathcal{T}} t^2 ||\mathbf{v}_p||,$$

where n_D is the number of pulses and $\mathbf{v}_p$ is the platform velocity vector. Note that $\mathcal{A}$ is the mean squared virtual aperture size and ρ is the mean square synthetic aperture size (i.e., the aperture formed by the set of the different transmit locations).

For a given target velocity $\mathbf{v}_t$ and unit direction vector $\mathbf{u}$, under certain assumptions (made explicit in [8]) one can show that the following approximation holds

$$\mathbf{v}_t \cdot \mathbf{u} \approx \frac{2}{\pi} \arcsin \sqrt{\mathrm{SINR}_{\mathrm{loss}}} ||\mathbf{v}_p|| \sqrt{\mathcal{A}^{-1} + \rho^{-1}}. \tag{21}$$

SINR loss curves can be constructed by using this relationship to solve for the target Doppler for a given set of SINR loss values. The relationship in (21) thus expresses the SINR loss as a function of both the virtual (spatial) and synthetic (temporal) apertures.

The values of $\mathcal{A}$ and ρ for the configurations used in the experiment are shown in Table 3. Although the additional integration time of the DDMA SIMO does increase its ρ value, it can be

seen that the system is primarily aperture limited, so longer integration would not be expected to produce much of an improvement in SINR loss performance. This can be seen visually by looking at the theoretical SINR loss plots for the DDMA SIMO and Conventional SIMO shown in Figure 37. They can be seen to be essentially identical.

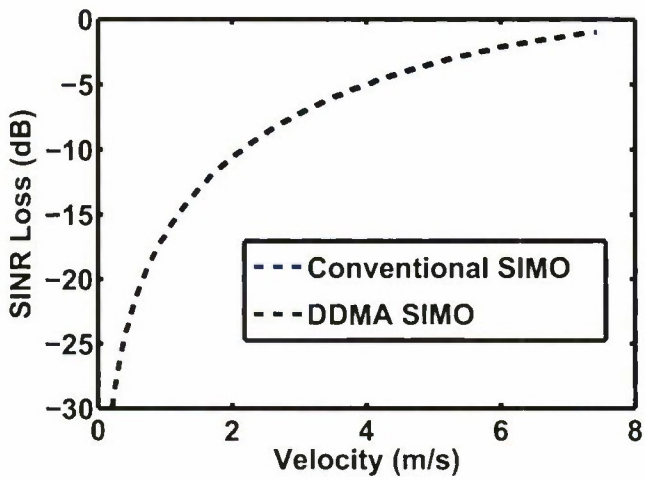

Figure 37. Conventional and DDMA SIMO theoretical SINR loss.

TABLE 3
$\mathcal{A}$ and ρ for Different Array Configurations

	$\mathcal{A}$	ρ
DDMA and TDMA MIMO	769.3	19048.569
DDMA SIMO	45.12	19048.569
Conventional SIMO	45.12	1190.54

Consider again the SINR loss plot from Figure 28. It is natural to wonder about the variation in performance of the MIMO and SIMO systems. It appears that the DDMA MIMO slightly outperforms the TDMA MIMO. However, note that the TDMA data was not interleaved with the DDMA data and in fact was recorded on a completely different pass with different aircraft conditions (crab, etc.), which are probably responsible for the difference in performance. Next note that the conventional SIMO is not quite as good as the DDMA SIMO. As we have just discussed, the increased integration time of the DDMA SIMO cannot be responsible for its enhanced performance. We suspect these differences are likely due to calibration issues.

Another possible source of SINR loss degradation is range ambiguities. The system's maximum

unambiguous range was approximately 22 km. Looking at the data, it seems that the returns had reached the noise floor by that point. However, it is possible that there is an elevation sidelobe contributing some range ambiguities to the near in range bins that is not directly visible.

Although all processing methods would be experiencing range ambiguities, we expect DDMA MIMO and DDMA SIMO to be affected much less by range ambiguities. This is because the variation from pulse to pulse in the transmitted signal effectively codes range ambiguous targets differently than unambiguous ones. For the DDMA MIMO processing, this effectively forces range-ambiguous targets off the array manifold. For the DDMA SIMO, the interleaved CPI structure means that range ambiguous returns will generally be coming from a different angle than the direction the beam is steered to on the subsequent pulse.

Let us also consider the detection performance of the conventional SIMO data in comparison to the DDMA SIMO data. The conventional scanning approach requires a shorter CPI, so the Doppler resolution is reduced by a factor of n_T; however, the unambiguous Doppler space is n_T times wider, allowing for a greater range of unambiguous velocities. From a detection perspective, the reduced Doppler resolution increases the clutter-to-noise ratio in a range-Doppler cell which can degrade detection performance. The combination of increased clutter-to-noise ratio combined with the previously noted sub-par SINR loss performance, results in the poor performance for the conventional SIMO system indicated in Figure 22.

The TDMA data was not interleaved with the DDMA MIMO data so we cannot directly compare the detection performance, however, it seemed to have similar detection capability to the DDMA MIMO system. Due to the different vehicle positions and shadowing effects, it is difficult to make a more precise statement. Note that the TDMA waveforms have 6 dB less SNR than the DDMA waveforms (however, the CNR is also reduced by 6 dB).

Next, recall that the SIMO examples shown up to this point were configured with a dense transmit and dense receive array and the MIMO examples were configured with a dense transmit and sparse receive array. For SIMO, dense arrays are critical for avoiding adverse effects of grating lobes, in particular blind speeds and angle ambiguities. However, the dense array restricts the aperture size of the SIMO system in comparison to the MIMO system. It is true that the larger sparse aperture used by the MIMO system is the driving factor behind its superior performance. If one is willing to deal with blind speeds and angle ambiguities, then one could use a sparse array in a conventional SIMO system to achieve nearly the same angle resolution and MDV as the MIMO system. On the other hand, if the physical size of the radar is strictly constrained (as it may be for a pod-based radar), then one may also want to consider a MIMO system using only the densely packed array aperture. We compare the SINR loss curves for all four of these configurations in Figure 38.

As seen in Figure 38, the sparse SIMO system achieves the same narrow clutter notch as the sparse MIMO system at the expense of multiple blind speeds. Due to the narrow clutter notch, the sparse SIMO system has comparable detection performance to the sparse MIMO system for the targets in our test area because they are all slow moving (2–6 m/s). Although we did not have experimental targets moving fast enough to demonstrate this, it is clear from Figure 38, that targets traveling with a radial velocity around ± 12 m/s (and at an angle of 0 relative to broadside) would

be invisible to the SIMO system in this configuration due to the grating lobes.

Blind velocities could be mitigated by collecting data with multiple PRFs. In this manner, one could conceivably construct a sparse SIMO system and use PRF agility to reduce blind speeds and angle ambiguities at the expense of longer dwell times.

Next, compare the dense SIMO to the dense MIMO configuration. Both the transmit and receive arrays are dense so there are no blind speeds. However, the dense MIMO virtual array is nearly twice the length of the dense SIMO receive array which does afford a noticeable improvement in SINR loss for slow movers. Note that due to the redundant phase centers, the dense MIMO effectively has a triangular taper applied to it that will widen its notch somewhat (while providing lower sidelobes). By weighting the elements appropriately this taper could be removed which would narrow its notch a bit further.

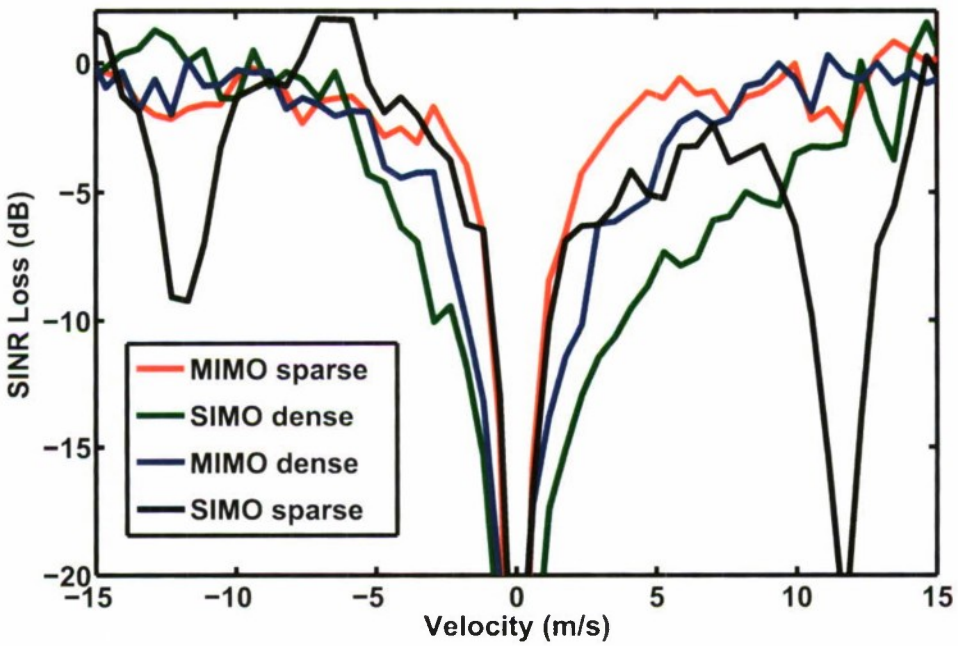

Figure 38. SINR loss curves for different array configurations at azimuthal angle 0.

Lastly, we should point out that the relationship between the DDMA MIMO waveforms and the interleaved SIMO operation, which held in this example collection, need not hold in general. The DDMA waveforms could be applied to an irregularly spaced transmit array or the waveform order over the transmit modules could be permuted and the result would not correspond to a

standard SIMO configuration.

7.1 RECOMMENDED MIMO SCENARIOS

Having compared different options for MIMO vs SIMO, a natural question to ask is when to use MIMO. Many articles and reports concerning MIMO seem to give the impression that MIMO is always better. One might be led to conclude that a MIMO radar is always better than a conventional radar. This of course is too simplistic. It is important to note that there is one curve that would be useful to have in Figure 38, which we do not have data for. That would be the SINR loss performance for a large filled conventional SIMO array with 16 receive phase centers at the same locations as the virtual array phase centers of the sparse MIMO configuration. Although we don't have actual data for it, it should perform at least as good as the sparse MIMO. In fact, we expect that a MIMO system will inevitably incur a couple dB of processing loss that a conventional array would not, so the large filled conventional array would probably outperform the sparse MIMO system. The large conventional array could also be operated at a lower PRF as we have mentioned. The main disadvantage of the conventional array is that it is larger, heavier, and requires more receiver and transmitter components.

To assess the applicability of MIMO to a given problem one first needs to consider if the platform and budget supports a physical array large enough to meet the radar performance requirements. If it does, then a conventional array of the appropriate size will perform at least as well, if not better than a MIMO system whose virtual array phase centers are at the same locations as the conventional systems physical phase centers.

One the other hand, there will be situations where performance requirements lead one to an array that the platform physically cannot support. This is likely to be the case with smaller UAV platforms, as well as with arrays operating at longer wavelengths. In this case, MIMO may let one synthesize a virtual array which can yield the desired performance, in a package which has an acceptable SWaP. Scenarios of this type where MIMO may be the only usable option capable of yielding the desired performance are likely the best fit for real-world MIMO systems. Note that the MIMO performance does not come without cost. A MIMO system in a worst case scenario requires n_T more pulse compressions, n_T more Doppler filters, and STAP using n_T more degrees of freedom. Luckily, silicon tends to be cheap and get cheaper. A more serious limitation is the fact that the best waveforms that we know of for MIMO systems require higher PRFs than conventional system. This limits them to closer in operation at higher grazing angles. Performance at long ranges and low grazing angles will be degraded by range ambiguities and eclipsing. This can be avoided to some extent by designing arrays with taller apertures to minimize or null elevation sidelobes.

Even if the platform supports a filled conventional array, it may be that a cheaper array yielding similar performance could be constructed using MIMO techniques to reduce the physical number of phase centers. A discussion of cost comparisons for MIMO and SIMO system can be found in [17].

Lastly, one possible application of MIMO is as a technique to improve the performance of existing systems. Here we are considering situations where existing assets not initially designed for

MIMO, might be operated in a MIMO fashion. In particular, multiple existing radars with smaller apertures could be combined using MIMO to synthesize a large virtual array.

8. FUTURE WORK

There are a few fronts on which we would like to see future work at Lincoln Laboratory on MIMO GMTI proceed. Overall the experiment validated our theoretical models and understanding of MIMO systems. This gives us good confidence in the collection of MIMO modeling tools we have developed, in particular our MIMO GMTI simulator. The simulator is quite general and allows us to explore and compare the performance of systems employing very general array geometries and waveforms. We have been doing simulation work to assess the expected performance of some initial concepts for incorporating MIMO radar into real-world systems.

8.1 IMPROVED CALIBRATION METHODOLOGY

An interesting and to our knowledge unexplored aspect of practical MIMO systems concerns the calibration procedure for MIMO radars. As we have mentioned, in contrast to conventional radars, MIMO systems allow for calibration of the transmitters after the data has been recorded. As described in Section 5, we developed an adaptive calibration approach using the ground clutter. We found the calibration stage was absolutely crucial for extracting any meaningful results from the data.

We envision that a real-world MIMO system would have some facility to record the output of each transmitter and would then use this data stream in a calibration stage to correct for errors and mismatches between the transmitters. Experimental or simulation work along these lines may be useful.

8.2 WAVEFORM DESIGN

In spite of a relatively large body of research on MIMO radar, the central problem of finding good MIMO waveforms is still quite open. As we have shown the DDMA/TDMA waveforms yield good performance, however, one would hope there is a larger class of waveforms that can support good performance. As we have described in Section 2, there are signficant restrictions on GMTI MIMO waveforms to maintain low clutter rank thus this is not a simple problem. We believe further research to develop waveforms and processing tecniques for MIMO waveforms would be useful.

8.3 POSSIBLE MODIFICATIONS TO EXISTING HARDWARE FOR FUTURE DATA COLLECTION

Although the initial data collection was successful there were some limitations of the testbed and the test site that made some of the performance comparisons difficult. We have compiled a list of possible modifications to the existing testbed that it might be possible to implement at a low cost for a future data collection. The most important of these modfications would be increasing the

bandwidth from 10 Mhz to 20 MHz[6], doubling the transmit power[7] and adding time stamps to the receiver data to facilitate synchronization with the navigation data.

[6] The maxmum receiver bandwidth is 20 Mhz, and the maximum transmitter bandwidth is 30 Mhz. We were having some reliability issues with transmitters that the higher bandwidth seemed to exacerbate so to be safe the inital experiment was done using the 10 Mhz of bandwidth.

[7] We drove the power amplifiers at 25 W, but they have been tested by the manufacturer up to 50 W.

9. SUMMARY AND CONCLUSION

An airborne MIMO GMTI experiment has been conducted to demonstrate the potential for enhanced GMTI performance using MIMO techniques. In this report, we gave an overview of the theory of MIMO radars and documented the signal processing chain developed for our experimental data. We compared the experimental performance of the MIMO operation to the performance of the testbed operated in a conventional fashion. Overall, the MIMO system exhibited the expected performance gains predicted by theoretical analysis.

In particular, qualitative analysis of the post-STAP range-Doppler images clearly showed the improved detection performance of the MIMO systems. ROC curves were generated quantitatively showing the overall improved detection performance of the MIMO approach. Analysis of the SINR loss curves based on experimental data shows that the measured losses are close to the theoretical bounds predicted in [8]. Analysis of the data indicates the improved angle estimation performance of the MIMO system over the SIMO system, however, limitations of the testbed made precise comparisons difficult.

Throughout this report and in particular in Section 7, we tried to convey the subtlely involved in comparisons between MIMO and SIMO systems. We hope the reader did not leave with the impression that a MIMO system is always the right choice for optimal performance. Instead, our view is that MIMO is a powerful technique which in certain circumstances can yield performance difficult to achieve any other way, but which also has limitations which must be kept in mind.

This page intentionally left blank.

LIST OF ABBREVIATIONS AND ACRONYMS

Abbreviation	Description
MIMO	multiple-input multiple-output
SIMO	single-input multiple-output
GMTI	ground moving target indicator
MDV	minimum detectable velocity
SINR	signal-to-inference-plus-noise ratio
DDMA	Doppler-division multiple access
TDMA	time-division multiple access
MVDR	minimum variance distortionless response
AMF	adaptive matched filter

This page intentionally left blank.

REFERENCES

[1] J. Li and P. Stoica, Eds., *MIMO Radar Signal Processing.* New York: Wiley, 2009.

[2] C.-Y. Chen and P. Vaidyanathan, "MIMO Radar Space-Time Adaptive Processing Using Prolate Spheroidal Wave Functions," *Signal Processing, IEEE Transactions on*, vol. 56, no. 2, pp. 623–635, Feb. 2008.

[3] M. Xue, X. Zhu, J. Li, D. Vu, and P. Stoica, "MIMO radar angle-doppler imaging via iterative space-time adaptive processing," in *Waveform Diversity and Design Conference, 2009 International*, Feb. 2009, pp. 129–133.

[4] D. Rabideau and P. Parker, "Ubiquitous MIMO multifunction digital array radar," in *Signals, Systems and Computers, 2003. Conference Record of the Thirty-Seventh Asilomar Conference on*, vol. 1, 2003, pp. 1057–1064.

[5] E. Fishler, A. Haimovich, R. Blum, D. Chizhik, L. Cimini, and R. Valenzuela, "MIMO radar: an idea whose time has come," in *Radar Conference, 2004. Proceedings of the IEEE*, Apr. 2004, pp. 71–78.

[6] F. Robey, S. Coutts, D. Weikle, J. McHarg, and K. Cuomo, "MIMO radar theory and experimental results," in *Signals, Systems and Computers, 2004. Conference Record of the Thirty-Eighth Asilomar Conference on*, vol. 1, Nov. 2004, pp. 300–304.

[7] D. Bliss and K. Forsythe, "Multiple-input multiple-output (MIMO) radar and imaging: degrees of freedom and resolution," in *Signals, Systems and Computers, 2003. Conference Record of the Thirty-Seventh Asilomar Conference on*, vol. 1, Nov. 2003, pp. 54–59.

[8] K. W. Forsythe and D. W. Bliss, "MIMO radar: concepts, performance enhancements, and applications," in *MIMO Radar Signal Processing, J. Li and P. Stoica, Eds.* New York: Wiley, 2009.

[9] D. Bliss, K. Forsythe, S. Davis, G. Fawcett, D. Rabideau, L. Horowitz, and S. Kraut, "GMTI MIMO radar," in *Waveform Diversity and Design Conference, 2009 International*, Feb. 2009, pp. 118–122.

[10] K. Forsythe and D. Bliss, "MIMO Radar Waveform Constraints for GMTI," *Selected Topics in Signal Processing, IEEE Journal of*, vol. 4, no. 1, pp. 21–32, Feb. 2010.

[11] D. J. Rabideau, "Adaptive MIMO radar waveforms," *Proceedings of the IEEE Radar Conference*, pp. 1–6, May 2008.

[12] V. Mecca and J. Krolik, "Slow-Time MIMO STAP with Improved Power Efficiency," in *Signals, Systems and Computers, 2007. ACSSC 2007. Conference Record of the Forty-First Asilomar Conference on*, Nov. 2007, pp. 202–206.

[13] L. Horowitz, "Clutter cancellation limits of adaptive processing applied to coherent MIMO GMTI," *MIT Lincoln Laboratory, Tech. Rep. TR-1132*, DATE TBD.

[14] J. Ward, "Space-time adaptive processing for airborne radar," *MIT Lincoln Laboratory, Tech. Rep. TR-1015*, Dec. 1994.

[15] S. Kogon and M. Zatman, "STAP adaptive weight training using phase and power selection criteria," *Conference Record of the Thirty-Fifth Asilomar Conference of Signals, Systems, and Computers*, vol. 1, pp. 98–102, Nov. 2001.

[16] D. Rabideau and A. Steinhardt, "Improved adaptive clutter cancellation through data-adaptive training," *Aerospace and Electronic Systems, IEEE Transactions on*, pp. 879–891, Jul. 1999.

[17] D. J. Rabideau, "MIMO radar aperture optimization," *MIT Lincoln Laboratory, Tech. Rep. TR-1149*, Date TBD.

REPORT DOCUMENTATION PAGE

Form Approved
OMB No. 0704-0188

1. REPORT DATE	2. REPORT TYPE	3. DATES COVERED *(From - To)*
31 March 2011	Technical Report	

4. TITLE AND SUBTITLE

Airborne MIMO GMTI Radar

5a. CONTRACT NUMBER
FA8721-05-C-0002

5b. GRANT NUMBER

5c. PROGRAM ELEMENT NUMBER

6. AUTHOR(S)

J.M. Kantor and Shakti Davis, Group 105

5d. PROJECT NUMBER
2222

5e. TASK NUMBER
9031

5f. WORK UNIT NUMBER

7. PERFORMING ORGANIZATION NAME(S) AND ADDRESS(ES) AND ADDRESS(ES)

MIT Lincoln Laboratory
244 Wood Street
Lexington, MA 02420-9108

8. PERFORMING ORGANIZATION REPORT NUMBER
TR-1150

9. SPONSORING / MONITORING AGENCY NAME(S) AND ADDRESS(ES)

Air Force ESC/CAA
20 Schilling Circle
Hanscom AFB, MA 01731

10. SPONSOR/MONITOR'S ACRONYM(S)

11. SPONSOR/MONITOR'S REPORT NUMBER(S)
ESC-TR-2010-054

12. DISTRIBUTION / AVAILABILITY STATEMENT

Approved for public release; distribution is unlimited.

13. SUPPLEMENTARY NOTES

14. ABSTRACT

The performance of a ground moving target indicator (GMTI) radar is strongly driven by the length of the radar aperture, as longer apertures enable lower minimum detectable velocity (MDV) and better target geolocation. Multiple-input multiple-output (MIMO) techniques can enable the use of long sparse array geometries while avoiding the adverse sidelobe effects typical of such arrays. In 2009, an experiment was conducted at Ft. Devens, Massachusetts, to collect MIMO GMTI data on instrumented ground targets. A reconfigurable S-band antenna array was programmed to transmit both conventional single-input multiple-output (SIMO) and MIMO waveforms. Analysis of the data indicates improved detection performance with the MIMO techniques compared to the conventional SIMO approach as well as improved geolocation capability.

15. SUBJECT TERMS

16. SECURITY CLASSIFICATION OF:			17. LIMITATION OF ABSTRACT	18. NUMBER OF PAGES	19a. NAME OF RESPONSIBLE PERSON
a. REPORT	b. ABSTRACT	c. THIS PAGE	Same as report	68	19b. TELEPHONE NUMBER *(include area code)*
Unclassified	Unclassified	Unclassified			

This page intentionally left blank.